Secrecy-Rate Optimization of Double RIS-Aided Space-Ground Networks

Tiep M. Hoang, Chao Xu, Alireza Vahid, Hoang Duong Tuan, Trung Q. Duong, and Lajos Hanzo, *Life Fellow, IEEE*

***Abstract*—The physical layer security (PLS) of a space-ground communication system is examined. To improve the security performance, a pair of reconfigurable intelligent surfaces (RISs) is integrated into the system and benchmarked against a scheme, where there is only a single RIS close to the ground station. As for the double-RIS scenario, we formulate a secrecy rate maximization problem, and then propose an alternating optimization (AO) algorithm for jointly optimizing three vectors, namely the beamformer of the ground station and the reflecting vectors of two different RISs. Similarly, as for the single-RIS case, we also propose another AO algorithm for optimizing a pair of vectors, namely the beamformer of the ground station and the reflecting vector of the single RIS. Both the double-RIS and the single-RIS AO algorithms are developed on the basis of the first-order Taylor expansion and the Dinkelbach's method, which allow us to approximate non-convex optimization problems by convex ones. Our results demonstrate that the proposed double-RIS scheme outperforms the single-RIS benchmark scheme in terms of its security.**

***Index terms*—**Physical layer security, reconfigurable intelligent surface, alternating optimization, space-ground network.

I. Introduction

Recently, space-air-ground integrated networks (SAGINs) have been conceived to include a diverse range of flying objects, such as satellites, aeroplanes and unmanned aerial vehicles (UAVs) [1]–[3], in order to expand the coverage area and for constructing the Internet of flying objects. To clarify the terminology, SAGINs are constituted by an aeronautical ah-hoc networks (AANETs) relying on aeroplanes, on flying ah-hoc network (FANETs) of UAVs, and satellite-terrestrial networks.[1] Furthermore, SAGINs are also envisioned to support the ubiquitous Internet of Things (IoT) [4]. To enhance the system performance attained, it is envisioned that reconfigurable intelligent surfaces (RISs) will also be integrated into SAGINs in the sixth-generation (6G) communication systems [5]. For instance, [6] shows that a satellite-terrestrial system using RISs efficiently improves the resource utilization and maximizes the total revenue within a limited coverage area.

However, owing to the broadcast nature of wireless propagation, the information transmission in SAGINs is vulnerable to potential eavesdroppers [7]. Hence, the physical-layer (PHY) security and authentication in wireless systems have become compelling research topics. Since wireless systems constantly evolve over time, new security challenges and requirements continue to arise. Thus, the diversity of the recently-developed SAGIN architectures will also lead to the diversity of PHY security solutions, but there is a paucity of literature on this wide open research topic. As an attractive PHY enhancement technique, reconfigurable intelligent surfaces (RISs) have shown substantial potential in improving wireless systems, including but not limited to channel capacity enhancements [8], energy-efficiency versus spectral-efficiency trade-off [9], and so on. Hence, RIS-aided PHY security is also a topic of salient interest [10]–[23]. As a benefit, RISs are capable of creating additional propagation paths between a pair of transceivers by beneficially adjusting the reflected signal phases through software for improving the achievable rate [8]. Moreover, if a wireless system is equipped with a pair of Tx-Rx RISs, both the spectral efficiency and the coverage of the system may be improved [24]. Indeed, having more RIS panels may be expected to glean more energy at the receiver, but positioning a pair of them strategically, one in the vicinity of the transmitter and one near the receiver is recommended [25]. This is because a single RIS provides good reception at the base station, but not at the destination. However, in the presence of eavesdroppers, it is not clear how RISs can improve security. Although the authors of [10]–[23] addressed some of the relevant security issues, there are numerous open problems in practical scenarios.

A. State-of-the-art

As one of the first contributions on RIS-aided PHY security, Yang *et al.* [10] propose an RIS-aided system and analyze its secrecy outage probability. In [11], Tang *et al.* consider a non-orthogonal multiple access (NOMA) network integrated with an RIS and analyzed its PHY security. Similar to [11], Zhang *et al.* [12] also study the PHY security of an RIS-aided NOMA network under the assumption of having no line-of-sight paths. Upon considering a similar setup, Luo *et al.* [13] evaluate the impact of RISs on the security by analyzing the degree of randomness, spectral efficiency and reliability. Indeed, one of

T. M. Hoang and A. Vahid are with the Department of Electrical Engineering, the University of Colorado Denver, Denver, CO 80204, USA (e-mails: minhtiep.hoang@ucdenver.edu; alireza.vahid@ucdenver.edu).

C. Xu and L. Hanzo are with the School of Electronics and Computer Science, the University of Southampton, Southampton SO17 1BJ, U.K. (e-mails: cx1g08@ecs.soton.ac.uk; lh@ecs.soton.ac.uk).

H. D. Tuan is with the School of Electrical and Data Engineering, University of Technology Sydney, Ultimo, NSW 2007, Australia (e-mail: tuan.hoang@uts.edu.au).

T. Q. Duong is with the School of Electronics, Electrical Engineering and Computer Science, the Queen's University of Belfast, Belfast BT7 1NN, U.K. (e-mail: trung.q.duong@qub.ac.uk).

The work of Tiep M. Hoang and Alireza Vahid was in part supported by NSF grants ECCS-2030285, CNS-2106692, and CNS-2211804.

L. Hanzo would like to acknowledge the financial support of the Engineering and Physical Sciences Research Council projects EP/W016605/1 and EP/X01228X/1 as well as of the European Research Council's Advanced Fellow Grant QuantCom (Grant No. 789028)

[1]A detailed distinction between AANETs and FANETs is provided in [3].

TABLE I
CONTRASTING OUR CONTRIBUTIONS TO THE LITERATURE

	[22]	[23]	[20]	[21]	[19]	[27]	[28]	[24]	[29]	[30]	This
Double-RIS aided systems	✓	✓						✓			✓
Reflection between two RISs	✓							✓			✓
PHY security	✓	✓	✓	✓	✓				✓		✓
Space-ground communication						✓	✓		✓	✓	✓
Space-air-ground integrated networks						✓			✓	✓	✓
Rician fading					✓	✓				✓	✓
Joint optimization	✓		✓	✓	✓			✓	✓	✓	✓
Temporal correlation in flying ad-hoc scenario											✓
Spatial correlation among RIS elements											✓

the main advantages of an RIS is the ability to beneficially adjust phase shifts but no detailed RIS phase shift optimization was considered in [10]–[13].

With the objective of maximizing the security level of RIS-aided wireless systems, some authors have designed formal optimization methods. To be more specific, Zhang *et al.* [14] apply stochastic geometry for modelling the presence of blockages and analyze the secrecy outage probability and the average secrecy rate. In [15], Dong *et al.* consider the RIS's ability to adjust the signal's amplitude for compensating the severe pathloss of the cascaded RIS channels, and then optimize the security level using an alternating optimization algorithm (AO). On the other hand, Hong *et al.* [16] propose a secrecy rate maximization technique relying on the optimization of the transmit precoding (TPC) matrix, the artificial noise covariance and the RIS phase shifts. To deal with this challenging problem, Hong *et al.* [16] develop a sophisticated algorithm based on block coordinate descent and majorization-minimization techniques. Similar to [16], Tang *et al.* [17] use a block coordinate descent technique; however, in contrast to the above-mentioned contributions, Tang *et al.* [17] introduce the so-called jamming signals for confusing the eavesdroppers. The employment of AO algorithms for joint optimization is also seen in [20] and [21], where Shu *et al.* [20] additionally take directional modulation into account, while Shi *et al.* [21] additionally consider the aspects of energy harvesting. On the other hand, Su. *et al.* [26] use an RIS for reflecting jamming signals to eavesdroppers in order to minimize the leakage of confidential information.

However, all the contributions in [10]–[17] and [20]–[23] consider terrestrial networks rather than SAGINs. In other words, none of them study secure transmissions between transceivers on the ground and in the air. On the other hand, to address the issues specific to air-ground transmission, the authors of [18] and [19] conceive secure UAV communications with the aid of RISs. Indeed, [18] and [19] propose similar network topologies. However, [18] only considers downlink transmission, while [19] considers both the downlink and uplink. Indeed, at the time of writing this manuscript, there is a paucity of literature on the PHY security of space-ground communications. Although UAV communications and space-ground communications may be combined into some rudimentary SAGINs, there are differences in path-loss modelling, spatial modelling and Doppler shift. In [31], an RIS-aided satellite system is studied and its power consumption is minimized through beneficially controlling the RIS coefficients, but the PHY security is not considered. Upon considering space-ground communications, the authors of [27] and [28] employ a single RIS either at the satellite or on the ground for supporting transmission over a long distance; but again, the topic of PLS is not the focus of [27] and [28]. On the other hand, Niu *et al.* [29] focus their attention on the security of a cognitive satellite-terrestrial network in the presence of eavesdroppers, where a single RIS is deployed on the ground. In [29], the AO algorithm is employed for dealing with the associated joint optimization of beamforming, artificial noise and RIS designs. The results in [29] show that the benefit of RISs is more substantial than that of artificial noise. Similarly, Lin *et al.* [30] study a single-RIS-aided satellite-terrestrial relay network, where the RIS is assumed to allow the signals to penetrate its surface. However, the associated security aspects are not investigated in [30].

Furthermore, none of the authors of [10]–[21], [29], [30] study the deployment of multiple RISs for securing transmissions. Thus, the pivotal question arises: whether or not multiple RISs are capable of guaranteeing more secure transmissions in the face of eavesdroppers? To partially address this open research question, Dong *et al.* [22] are the only authors using a pair of RISs to support secure transmission in the absence of line-of-sight (LoS) paths and show the potential of double RISs in terms of the PHY security. However, Dong *et al.* [22] only consider terrestrial communications, while in complete contrast, we study the challenging scenario of space-ground communications that normally includes LoS paths [22]. Moreover, the practical considerations associated both with the high velocities of satellites and with the spatial arrangement of RIS elements are also addressed in our work. In contrast to [23], our study considers the placement of two RISs in front of each other to arrange for reflection between them. Furthermore, the arrangement of two RISs in [23] does not create reflection between the two RISs due to the lack of a propagation path from one RIS to the other. Additionally, the practical assumptions of having both temporal and spatial correlations are also absent from the analysis in [23].

Our contributions are boldly and explicitly contrasted to the literature at a glance in Table I.

B. Our Main Contributions

To elaborate, our main contributions can be summarized as follows:

- We study a novel space-ground communication system, which belongs to the family of of SAGINs, relying on

the integration of a pair of RISs. Moreover, we consider a range of practical assumptions ignored by most of the previous literature, such as the coexistence of both LoS and non-line-of-sight (NLoS) paths, the Doppler effect imposed on the temporal correlation, and the spatial configuration of RIS elements.

- Then, we study the potential of double RISs in improving the security performance, which is also ignored by most of the previous works (i.e., [10]–[19]). Furthermore, we also consider a benchmark scheme, where our space-ground communication system only employs a single RIS at the source. Our double-RIS scheme advocated is compared to a single-RIS scheme.
- Specially, to maximize the secrecy rate of the proposed system, we rely on the first-order Taylor expansion and on Dinkelbach's method to develop two variants of our AO algorithms. To be more specific, the so-called double-RIS AO algorithm is used as part of the double-RIS scheme for jointly optimizing the beamforming vector at the source and the two reflecting matrices at two different RISs. By contrast, the so-called single-RIS AO algorithm is used in the single-RIS scheme for jointly optimizing the beamforming vector and the single reflecting vector.

The rest of this paper is organized as follows. Section II presents the proposed double RIS-aided space-ground network. In Section III, we formulate our secrecy maximization problem and propose the double-RIS AO algorithm. In Section IV, we first present the benchmark scheme, where only a single RIS is deployed at the ground station, and then propose the single-RIS AO algorithm. Our numerical results are presented in Section V and finally, Section VI concludes the paper.

Notations: $\mathbb{R}^{m\times n}$ denotes the real field that includes all real-valued matrices of size $m \times n$; $\mathbb{C}^{m\times n}$ denotes the complex field that includes all complex-valued matrices of size $m \times n$; The operation $\text{diag}\left([z_1, \ldots, z_K]\right)$ diagonalizes a row vector $[z_1, \ldots, z_K]$ into a diagonal matrix; Bold lowercase letters and bold uppercase letters denote vectors and matrices, respectively; $\mathbf{I}_n$ denotes the identity matrix of size $n \times n$; The superscripts $(\cdot)^\top$, $(\cdot)^*$, and $(\cdot)^\dagger$ represent the transpose, conjugate, and Hermitian operators, respectively; $\Re\{\cdot\}$ denotes the real part of a complex-valued matrix; $\langle \mathbf{x}, \mathbf{y}\rangle = \mathbf{y}^\dagger\mathbf{x}$ denotes the inner product of a pair of complex vectors $\mathbf{x}$ and $\mathbf{y}$; $\mathbf{z} \sim \mathcal{CN}(\mathbf{m}, \mathbf{\Sigma})$ is a complex Gaussian random vector having a mean of $\mathbf{m}$ and covariance matrix $\mathbf{\Sigma}$; $\nabla_{\mathbf{z}} f(\mathbf{z})$ denotes the gradient of $f(\mathbf{z})$ with respect to (w.r.t.) $\mathbf{z}$; $\nabla_{\mathbf{z}} f(\mathbf{z})\big|_{\mathbf{z}=\mathbf{z}_0}$ represents the gradient of $f(\mathbf{z})$ evaluated at $\mathbf{z} = \mathbf{z}_0$.

II. System Model

A. Signal Modeling

Let us now consider a satellite-air-ground network (SAGN) consisting of a ground base station (A), a legitimate satellite (B) and an undesired satellite (E). We assume that A is transmitting confidential signals towards B in a scenario, where there is no the LoS component due to the surrounding buildings, trees and walls.[2] On the other hand, the eavesdropper (E) remains silent and tries to decode the confidential signals gleaned from A. To enhance the secure transmission between A and B, we employ a pair of RISs. To be more specific, the first RIS (R_1) is placed close to A, while the second RIS (R_2) is attached to B. Figure 1 illustrates our system model.

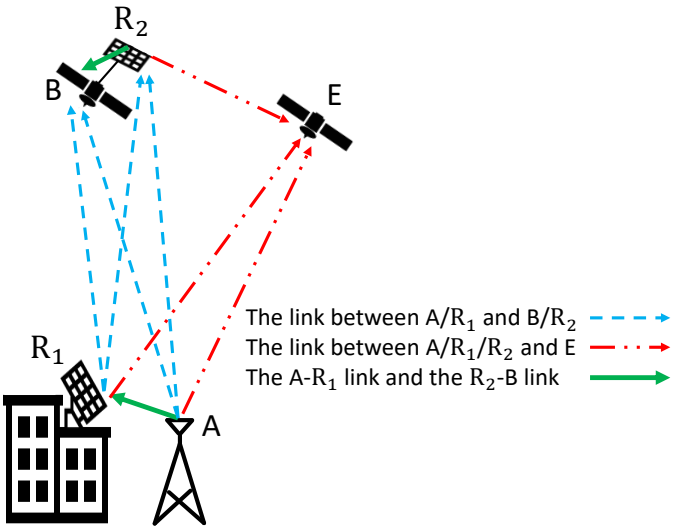

Fig. 1. System model.

Let us denote the signal intended for B by s, with the average transmit power being $\mathbb{E}\left\{|s|^2\right\} = P$. Upon denoting the beamforming vector by $\mathbf{w} \in \mathbb{C}^{L\times 1}$ with $\|\mathbf{w}\|^2 = \text{tr}(\mathbf{w}\mathbf{w}^\dagger) \leq 1$, the transmitted signal becomes $\mathbf{x} = \mathbf{w}s$. The signal received at B can be expressed as

$$\begin{aligned} y_B = &\sqrt{\Lambda_{BR_2}\Omega_{R_2R_1}\Omega_{R_1A}/\sigma_0}\ \mathbf{h}_{BR_2}\mathbf{R}_2\mathbf{H}_{R_2R_1}\mathbf{R}_1\mathbf{H}_{R_1A}\mathbf{w}s \\ &+ \sqrt{\Lambda_{BR_1}\Omega_{R_1A}/\sigma_0}\ \mathbf{h}_{BR_1}\mathbf{R}_1\mathbf{H}_{R_1A}\mathbf{w}s \\ &+ \sqrt{\Lambda_{BR_2}\Omega_{R_2A}/\sigma_0}\ \mathbf{h}_{BR_2}\mathbf{R}_2\mathbf{H}_{R_2A}\mathbf{w}s \\ &+ \sqrt{\Lambda_{BA}/\sigma_0}\ \mathbf{h}_{BA}\mathbf{w}s + n_B, \end{aligned} \tag{1}$$

where Λ_{XY} represents the path loss between a certain point X in the space/air and another point Y on the ground, Ω_{XY} represents the path loss between two points X and Y on the ground, $\mathbf{R}_1 = \text{diag}\left(\left[e^{j2\pi\theta_1}, \ldots, e^{j2\pi\theta_N}\right]\right)$ is the diagonal reflection matrix of R_1, $\mathbf{R}_2 = \text{diag}\left(\left[e^{j2\pi\phi_1}, \ldots, e^{j2\pi\phi_N}\right]\right)$ is the diagonal reflection matrix of R_2, $\mathbf{h}_{BR_1} \in \mathbb{C}^{1\times N}$ is the B-R_1 channel, $\mathbf{h}_{BR_2} \in \mathbb{C}^{1\times N}$ is the B-R_2 channel, $\mathbf{H}_{R_2R_1} = [\mathbf{h}_{1R_2}, \ldots, \mathbf{h}_{NR_2}] \in \mathbb{C}^{N\times N}$ is the R_2-R_1 channel, $\mathbf{H}_{R_1A} \in \mathbb{C}^{N\times L}$ is the R_1-A channel, $\mathbf{H}_{R_2A} \in \mathbb{C}^{N\times L}$ is the R_2-A channel, $\mathbf{h}_{BA} \in \mathbb{C}^{1\times L}$ is the B-A channel, σ_0 is the noise variance, and finally $n_B \sim \mathcal{CN}(0, 1)$ is the normalized additive white Gaussian noise (AWGN) at B. Note that the path loss models are described in Subsection II-B, while the RIS-related channel models of high-speed scenarios are described in Subsection II-C.

[2]It is also worth mentioning that if the distance between B and the ground is not sufficiently large, or if the distance between B and A is too high, then there may not exist a LoS path between B and A.

Similarly, the signal received at E can be expressed as

$$\begin{aligned} y_E = &\sqrt{\Lambda_{ER_2}\Omega_{R_2R_1}\Omega_{R_1A}/\sigma_0}\ \mathbf{h}_{ER_2}\mathbf{R}_2\mathbf{H}_{R_2R_1}\mathbf{R}_1\mathbf{H}_{R_1A}\mathbf{w}s \\ &+ \sqrt{\Lambda_{ER_1}\Omega_{R_1A}/\sigma_0}\ \mathbf{h}_{ER_1}\mathbf{R}_1\mathbf{H}_{R_1A}\mathbf{w}s \\ &+ \sqrt{\Lambda_{ER_2}\Omega_{R_2A}/\sigma_0}\ \mathbf{h}_{ER_2}\mathbf{R}_2\mathbf{H}_{R_2A}\mathbf{w}s \\ &+ \sqrt{\Lambda_{EA}/\sigma_0}\ \mathbf{h}_{EA}\mathbf{w}s + n_E, \end{aligned} \tag{2}$$

where $\mathbf{h}_{ER_1} \in \mathbb{C}^{1\times N}$ is the E-R_1 channel, $\mathbf{h}_{ER_2} \in \mathbb{C}^{1\times N}$ is the E-R_2 channel, $\mathbf{h}_{EA} \in \mathbb{C}^{1\times L}$ is the E-A channel, and $n_E \sim \mathcal{CN}(0,1)$ is the normalized AWGN at E.

Proposition 1. *Given a square matrix* $\mathbf{X}$ *and two column vectors* $\boldsymbol{\theta}$ *and* $\mathbf{z}$*, we have* $\mathbf{X}\mathrm{diag}(\boldsymbol{\theta})\,\mathbf{z} = \mathbf{X}\mathrm{diag}(\mathbf{z})\,\boldsymbol{\theta}$.

Proposition 2. *Let us assume that* $\mathrm{diag}(\boldsymbol{\phi})$ *is exactly the same as* $\mathrm{diag}\left(\boldsymbol{\phi}^\top\right)$*, i.e.* $\mathrm{diag}(\boldsymbol{\phi}) = \mathrm{diag}\left(\boldsymbol{\phi}^\top\right)$*. Given a square matrix* $\mathbf{X}$ *and two column vectors* $\boldsymbol{\phi}$ *and* $\mathbf{z}^\top$*, we have the fact that* $\mathbf{z}\ \mathrm{diag}(\boldsymbol{\phi})\,\mathbf{X} = \mathbf{z}\ \mathrm{diag}\left(\boldsymbol{\phi}^\top\right)\mathbf{X} = \boldsymbol{\phi}^\top\mathrm{diag}(\mathbf{z})\,\mathbf{X}$.

Proof. Both propositions can be readily proven after some manipulations. □

We first introduce $\boldsymbol{\theta}_1 = [\boldsymbol{\theta}_1(1),\ldots,\boldsymbol{\theta}_1(N)]^\top = \left[e^{j2\pi\theta_1},\ldots,e^{j2\pi\theta_N}\right]^\top \in \mathbb{C}^{N\times 1}$ and $\boldsymbol{\phi}_2 = [\boldsymbol{\phi}_2(1),\ldots,\boldsymbol{\phi}_2(N)]^\top = \left[e^{j2\pi\phi_1},\ldots,e^{j2\pi\phi_N}\right]^\top \in \mathbb{C}^{N\times 1}$ so that $\mathbf{R}_1 = \mathrm{diag}(\boldsymbol{\theta}_1)$ and $\mathbf{R}_2 = \mathrm{diag}(\boldsymbol{\phi}_2)$. Then, using Proposition 1, we can write

$$\mathbf{h}_{BR_1}\mathrm{diag}(\boldsymbol{\theta}_1)\,\mathbf{H}_{R_1A}\mathbf{w} = \mathbf{g}_{BR_1A}\boldsymbol{\theta}_1, \tag{3a}$$
$$\mathbf{h}_{BR_2}\mathrm{diag}(\boldsymbol{\phi}_2)\,\mathbf{H}_{R_2A}\mathbf{w} = \boldsymbol{\phi}_2^\top\mathbf{g}_{BR_2A}, \tag{3b}$$
$$\mathbf{h}_{ER_1}\mathrm{diag}(\boldsymbol{\theta}_1)\,\mathbf{H}_{R_1A}\mathbf{w} = \mathbf{g}_{ER_1A}\boldsymbol{\theta}_1, \tag{3c}$$
$$\mathbf{h}_{ER_2}\mathrm{diag}(\boldsymbol{\phi}_2)\,\mathbf{H}_{R_2A}\mathbf{w} = \boldsymbol{\phi}_2^\top\mathbf{g}_{ER_2A}, \tag{3d}$$

where

$$\begin{aligned} \mathbf{g}_{BR_1A} &= \mathbf{h}_{BR_1}\mathrm{diag}(\mathbf{H}_{R_1A}\mathbf{w}) \in \mathbb{C}^{1\times N}, \\ \mathbf{g}_{BR_2A} &= \mathrm{diag}(\mathbf{h}_{BR_2})\,\mathbf{H}_{R_2A}\mathbf{w} \in \mathbb{C}^{N\times 1}, \\ \mathbf{g}_{ER_1A} &= \mathbf{h}_{ER_1}\mathrm{diag}(\mathbf{H}_{R_1A}\mathbf{w}) \in \mathbb{C}^{1\times N}, \\ \mathbf{g}_{ER_2A} &= \mathrm{diag}(\mathbf{h}_{ER_2})\,\mathbf{H}_{R_2A}\mathbf{w} \in \mathbb{C}^{N\times 1}. \end{aligned}$$

Similarly, using both Propositions 1 and 2, we can write

$$\mathbf{h}_{BR_2}\mathrm{diag}(\boldsymbol{\phi}_2)\,\mathbf{H}_{R_2R_1}\mathrm{diag}(\boldsymbol{\theta}_1)\,\mathbf{H}_{R_1A}\mathbf{w} = \boldsymbol{\phi}_2^\top\mathbf{B}\boldsymbol{\theta}_1, \tag{4a}$$
$$\mathbf{h}_{ER_2}\mathrm{diag}(\boldsymbol{\phi}_2)\,\mathbf{H}_{R_2R_1}\mathrm{diag}(\boldsymbol{\theta}_1)\,\mathbf{H}_{R_1A}\mathbf{w} = \boldsymbol{\phi}_2^\top\mathbf{E}\boldsymbol{\theta}_1, \tag{4b}$$

where $\mathbf{B} = \mathrm{diag}(\mathbf{h}_{BR_2})\,\mathbf{H}_{R_2R_1}\mathrm{diag}(\mathbf{H}_{R_1A}\mathbf{w}) \in \mathbb{C}^{N\times N}$ and $\mathbf{E} = \mathrm{diag}(\mathbf{h}_{ER_2})\,\mathbf{H}_{R_2R_1}\mathrm{diag}(\mathbf{H}_{R_1A}\mathbf{w}) \in \mathbb{C}^{N\times N}$.

Upon substituting (3) and (4) into (1) and (2), we arrive at

$$\begin{aligned} y_B = &\xi_1\boldsymbol{\phi}_2^\top\mathbf{B}\boldsymbol{\theta}_1 s + \xi_2\mathbf{g}_{BR_1A}\boldsymbol{\theta}_1 s + \xi_3\boldsymbol{\phi}_2^\top\mathbf{g}_{BR_2A}s \\ &+ \xi_4\mathbf{h}_{BA}\mathbf{w}s + n_B, \end{aligned} \tag{5}$$

$$\begin{aligned} y_E = &\chi_1\boldsymbol{\phi}_2^\top\mathbf{E}\boldsymbol{\theta}_1 s + \chi_2\mathbf{g}_{ER_1A}\boldsymbol{\theta}_1 s + \chi_3\boldsymbol{\phi}_2^\top\mathbf{g}_{ER_2A}s \\ &+ \chi_4\mathbf{h}_{EA}\mathbf{w}s + n_E, \end{aligned} \tag{6}$$

where $\xi_1 = \sqrt{\Lambda_{BR_2}\Omega_{R_2R_1}\Omega_{R_1A}/\sigma_0}$, $\xi_2 = \sqrt{\Lambda_{BR_1}\Omega_{R_1A}/\sigma_0}$, $\xi_3 = \sqrt{\Lambda_{BR_2}\Omega_{R_2A}/\sigma_0}$, $\xi_4 = \sqrt{\Lambda_{BA}/\sigma_0}$, $\chi_1 = \sqrt{\Lambda_{ER_2}\Omega_{R_2R_1}\Omega_{R_1A}/\sigma_0}$, $\chi_2 = \sqrt{\Lambda_{ER_1}\Omega_{R_1A}/\sigma_0}$, $\chi_3 = \sqrt{\Lambda_{ER_2}\Omega_{R_2A}/\sigma_0}$, and $\chi_4 = \sqrt{\Lambda_{EA}/\sigma_0}$.

B. Path Loss Modeling

We will consider two different path loss models, namely the satellite-ground channels (or air-ground channels) and the other is for terrestrial channels. The path loss between a certain point X in the space/air and another point on the ground may be modeled as [32]

$$\Lambda_{XY} = -147.55 + 20\log_{10}(f_c) + 20\log_{10}(d_{XY}) + \mathrm{CL}, \tag{7}$$

where f_c (Hz) is the carrier frequency, and d_{XY} (m) is the distance between X and Y, while CL is the cluster loss that depends on the elevation angle between the satellite and the ground object, for instance, at an elevation of 60°, CL = 26.2 dB. By contrast, as for the pair of points X and Y on the ground, the path loss can be modelled as

$$\Omega_{XY} = -154.06 + 20\log_{10}(f_c) + 20\log_{10}(d_{XY}). \tag{8}$$

C. RIS-related Channel Modeling for High-speed Scenarios

1) Temporal Correlation: To clarify the notational usage in the rest of this paper, let us first consider an arbitrary channel $\mathbf{h}_{XY}(t) \in \mathbb{C}^{N\times 1}$ (or $\mathbf{h}_{XY}(t) \in \mathbb{C}^{1\times N}$) at time t between the points X and Y in a high-speed scenario, where N is the number of RIS elements. Since a line-of-sight (LoS) component may be present between a pair of network entities, we can use the Rician fading model to break $\mathbf{h}_{XY}(t)$ into

$$\mathbf{h}_{XY}(t) = \sqrt{\frac{K}{K+1}}\mathbf{h}_{XY}^{LoS}(t) + \sqrt{\frac{1}{K+1}}\mathbf{h}_{XY}^{NLoS}(t), \tag{9}$$

where $\{\cdot\}^{LoS}$ and $\{\cdot\}^{NLoS}$ represent the LoS and the non-line-of-sight (NLoS) components, respectively. In (9), $\mathbf{h}_{XY}^{LoS}(t)$ represents the actual LoS channel, while $\mathbf{h}_{XY}^{NLoS}(t)$ represents the actual NLoS channel at time t. As for the multipath delay, we denote $\widehat{\mathbf{h}}_{XY}^{NLoS}(t-\tau)$ as the estimate of $\mathbf{h}_{XY}^{NLoS}(t)$ at time $(t-\tau)$, with τ being the time delay. The time-domain correlation between $\mathbf{h}_{XY}^{NLoS}(t)$ and $\widehat{\mathbf{h}}_{XY}^{NLoS}(t-\tau)$ can be expressed as [33]:

$$\mathbf{h}_{XY}^{NLoS}(t) = \rho_{XY}\widehat{\mathbf{h}}_{XY}^{NLoS}(t-\tau) + \sqrt{1-\rho_{XY}^2}\mathbf{e}_{XY}(t), \tag{10}$$

where $\mathbf{e}_{XY}(t) \sim \mathcal{CN}(0,\mathbf{I})$ is the estimation error, and ρ_{XY} reflects the Doppler effect due to the high mobility of users in the system. Note that the channel estimate $\widehat{\mathbf{h}}_{XY}^{NLoS}$ differs from the actual channel $\mathbf{h}_{XY}^{NLoS}$, and the difference is modelled by an independent complex-valued Gaussian error.[3] It should be noted that the model of imperfect channel state information (CSI) in (10) is widely used in the literature as a benefit of its tractability (e.g., see [33], [35]). Moreover, we apply this model of imperfect CSI to every link between two arbitrary points X and Y. Using Jake's model [36], ρ_{XY} can be expressed as:

$$\rho_{XY} = J_0\left(2\pi f_c\vartheta_{XY}\tau/c_{\text{light}}\right) \tag{11}$$

[3]As for the eavesdropping links, perfect CSI knopwledge may be acquired when the eavesdropper is registered as a subscribed user [34]. Since every satellite has to register before commencing its operation, the knowledge of a malicious satellite's CSI may indeed be attained.

where $J_0(\cdot)$ is the zero-order Bessel function of the first kind, ϑ_{XY} is the relative velocity between X and Y, and c_{light} is the speed of light. We can assume $\widehat{\mathbf{h}}_{XY}^{NLoS}(t-\tau) \sim \mathcal{CN}\left(0, \widehat{\mathbf{R}}_{XY}\right)$ and generate the estimated samples using the Gaussian distribution. For readability, in the following we will drop time labels t and $(t-\tau)$.

2) Spatial Correlation: The estimate $\widehat{\mathbf{R}}_{XY}$ has to accurately characterize the actual *spatial correlation* among antenna/RIS elements, because the practical deployment of holographic MIMOs (as well as that of large intelligent surfaces) implies having the arrangement of an infinite number of elements in a *finite* space [37], [38]. With this in mind, in the sequel we will consider the spatial correlation among RIS elements using the recent findings of [39].

Let us assume that each RIS is a planar surface consisting of $N = N_0^2$ elements, where N_0 is the number of RIS elements along a horizontal/vertical edge. If $\delta\ell$ is the horizontal/vertical length of each RIS element, then the area of each RIS element is equal to $\mathcal{A} = (\delta\ell)^2$. According to [39], given an intensity attenuation μ, the (n,m)-th element of the correlation matrix $\widehat{\mathbf{R}}_{XY}$ can be modelled as:[4]

$$[\widehat{\mathbf{R}}]_{n,m} = \mu\mathcal{A}\frac{\sin\left(\frac{2\pi}{\lambda}\|\mathbf{u}_n - \mathbf{u}_m\|\right)}{\frac{2\pi}{\lambda}\|\mathbf{u}_n - \mathbf{u}_m\|}, \tag{12}$$

where $\mathbf{u}_n$ and $\mathbf{u}_m$ represent the locations of the n-th and m-th elements in the three-dimensional space, respectively. The difference $\mathbf{u}_n - \mathbf{u}_m$ can be calculated as

$$\mathbf{u}_n - \mathbf{u}_m = \begin{bmatrix} 0 \\ (\text{index}_n - \text{index}_m)\,\delta\ell \\ \left(\lfloor\frac{(n-1)}{N_0}\rfloor - \lfloor\frac{(m-1)}{N_0}\rfloor\right)\delta\ell \end{bmatrix}, \tag{13}$$

where the index_n (or index_m) represents the n-th element (or that of the m-th element), and $\lfloor\cdot\rfloor$ truncates the argument.

III. Security-Aware Capacity Maximization

A. Double-RIS Problem Formulation

From (5) and (6), we can deduce the instantaneous signal-to-noise ratios (SNRs) for B and E as follows:

$$\text{snr}_B = P \times \Big|\xi_1\boldsymbol{\phi}_2^\top\mathbf{B}\boldsymbol{\theta}_1 + \xi_2\mathbf{g}_{BR_1A}\boldsymbol{\theta}_1 + \xi_3\boldsymbol{\phi}_2^\top\mathbf{g}_{BR_2A} + \xi_4\mathbf{h}_{BA}\mathbf{w}\Big|^2, \tag{14}$$

$$\text{snr}_E = P \times \Big|\chi_1\boldsymbol{\phi}_2^\top\mathbf{E}\boldsymbol{\theta}_1 + \chi_2\mathbf{g}_{ER_1A}\boldsymbol{\theta}_1 + \chi_3\boldsymbol{\phi}_2^\top\mathbf{g}_{ER_2A} + \chi_4\mathbf{h}_{EA}\mathbf{w}\Big|^2. \tag{15}$$

The expressions in (14)–(15) facilitate the analysis with respect to $\boldsymbol{\theta}_1$ and $\boldsymbol{\phi}_2$, but they do not reveal the involvement of $\mathbf{w}$ in a tangible manner. Fortunately, to derive the SNRs that reveal the existence of $\mathbf{w}$, we can directly deduce the SNRs from (1)-(2) as follows:

$$\text{snr}_B = P\left|\mathbf{u}_{(\boldsymbol{\theta}_1,\boldsymbol{\phi}_2)}^\dagger\mathbf{w}\right|^2, \tag{16}$$

$$\text{snr}_E = P\left|\mathbf{v}_{(\boldsymbol{\theta}_1,\boldsymbol{\phi}_2)}^\dagger\mathbf{w}\right|^2, \tag{17}$$

[4]If the area $\mathcal{A}$ is small but the total RIS area $N\mathcal{A}$ theoretically goes to $+\infty$, then the rank of the correlation matrix approximately reaches $\pi N\mathcal{A}/\lambda^2$.

where $\mathbf{u}_{(\boldsymbol{\theta}_1,\boldsymbol{\phi}_2)}^\dagger$ and $\mathbf{v}_{(\boldsymbol{\theta}_1,\boldsymbol{\phi}_2)}^\dagger$ are 1-by-L row vectors, which are parameterized by $\boldsymbol{\theta}_1$ and $\boldsymbol{\phi}_2$. We have

$$\mathbf{u}_{(\boldsymbol{\theta}_1,\boldsymbol{\phi}_2)}^\dagger = \xi_1\mathbf{h}_{BR_2}\text{diag}\left(\boldsymbol{\phi}_2\right)\mathbf{H}_{R_2R_1}\text{diag}\left(\boldsymbol{\theta}_1\right)\mathbf{H}_{R_1A} + \xi_2\mathbf{h}_{BR_1}\text{diag}\left(\boldsymbol{\theta}_1\right)\mathbf{H}_{R_1A} + \xi_3\mathbf{h}_{BR_2}\text{diag}\left(\boldsymbol{\phi}_2\right)\mathbf{H}_{R_2A} + \xi_4\mathbf{h}_{BA} \tag{18}$$

and

$$\mathbf{v}_{(\boldsymbol{\theta}_1,\boldsymbol{\phi}_2)}^\dagger = \chi_1\mathbf{h}_{ER_2}\text{diag}\left(\boldsymbol{\phi}_2\right)\mathbf{H}_{R_2R_1}\text{diag}\left(\boldsymbol{\theta}_1\right)\mathbf{H}_{R_1A} + \chi_2\mathbf{h}_{ER_1}\text{diag}\left(\boldsymbol{\theta}_1\right)\mathbf{H}_{R_1A} + \chi_3\mathbf{h}_{ER_2}\text{diag}\left(\boldsymbol{\phi}_2\right)\mathbf{H}_{R_2A} + \chi_4\mathbf{h}_{EA}. \tag{19}$$

Remark 1. *Note that* (14) *and* (16) *are exactly the same. Furthermore,* (15) *and* (17) *are exactly the same. For a given* $\mathbf{w}$*, we will use* (14) *and* (15) *for analyzing the effect of* $\boldsymbol{\theta}_1$ *and* $\boldsymbol{\phi}_2$ *on the security performance. By contrast, for a given pair of* $(\boldsymbol{\theta}_1, \boldsymbol{\phi}_2)$*, we will use* (16) *and* (17) *for analyzing the effect* $\mathbf{w}$*.*

The legitimate capacity and the eavesdropping capacity in bits/s/Hz can be formulated as

$$C_B = \log_2\left(1 + \text{snr}_B\right), \tag{20}$$

$$C_E = \log_2\left(1 + \text{snr}_E\right). \tag{21}$$

Accordingly, it is well known that the achievable secrecy rate can be expressed as $C_s = \max(0, C_B - C_E)$, where $\max(0,z) = z$ for $z \geq 0$ and $\max(0,z) = 0$ for $z < 0$. In general, if the difference $C_B - C_E$ increases, it is likely to increase C_s and thus leading to a better security performance.

The security maximization problem can be formulated as:

$$\max_{\mathbf{w},\boldsymbol{\theta}_1,\boldsymbol{\phi}_2} \quad \log_2\left(\frac{1+\text{snr}_B}{1+\text{snr}_E}\right) \tag{22a}$$

$$\text{s.t.} \quad |\boldsymbol{\theta}_1(n)|^2 = 1,\ n \in \{1,\ldots,N\}, \tag{22b}$$

$$|\boldsymbol{\phi}_2(n)|^2 = 1,\ n \in \{1,\ldots,N\}, \tag{22c}$$

$$\text{tr}(\mathbf{w}\mathbf{w}^\dagger) = 1. \tag{22d}$$

Due to the monotonicity of the $\log_2(\cdot)$ function, maximizing $\log_2(z)$ is equivalent to maximizing z. Hence, the above problem can be equivalently rewritten as:

$$\max_{\mathbf{w},\boldsymbol{\theta}_1,\boldsymbol{\phi}_2} \quad \frac{1+\text{snr}_B}{1+\text{snr}_E} \tag{23a}$$

$$\text{s.t.} \quad \text{(22b), (22c), (22d).} \tag{23b}$$

B. Double-RIS AO Algorithm

In order to solve the optimization problem formulated above, we will employ the AO method, which solves multiple sub-algorithms iteratively. Instead of finding the optimal values of all the variables at the same time, which is almost impossible due to the complex relationship among them, the AO method allows us to deal with each variable at a time in an iterative manner. As for the k-th iteration, we denote the values of $\mathbf{w}$, $\boldsymbol{\theta}_1$ and $\boldsymbol{\phi}_2$ by $\mathbf{w}^{[k]}$, $\boldsymbol{\theta}_1^{[k]}$ and $\boldsymbol{\phi}_2^{[k]}$, respectively. To find the next value $\mathbf{w}^{[k+1]}$ of $\mathbf{w}$ at the $(k+1)$-th iteration, we first fix the pair of $(\boldsymbol{\theta}_1 = \boldsymbol{\theta}_1^{[k]}, \boldsymbol{\phi}_2 = \boldsymbol{\phi}_2^{[k]})$ and solve the sub-algorithm presented in Sub-section III-B1. Next, we fix the

pair of $(\mathbf{w}=\mathbf{w}^{[k+1]}, \boldsymbol{\phi}_2=\boldsymbol{\phi}_2^{[k]})$ and solve the sub-algorithm presented in Sub-section III-B2 to find the next value $\boldsymbol{\theta}_1^{[k+1]}$ of $\boldsymbol{\theta}_1$. Then, we fix the pair of $(\mathbf{w}=\mathbf{w}^{[k+1]}, \boldsymbol{\theta}_1=\boldsymbol{\theta}_1^{[k+1]})$ and solve the sub-algorithm presented in Sub-section III-B3 to find the next value $\boldsymbol{\phi}_2^{[k+1]}$ of $\boldsymbol{\phi}_2$. After multiple iterations, we can obtain an improved three-tuple $(\mathbf{w}, \boldsymbol{\theta}_1, \boldsymbol{\phi}_2)$ and terminate the AO algorithm based on the predetermined number of iterations, i.e. K_{iters}, or the predetermined error tolerance ϵ_{err}. In the sequel, the sub-algorithms will be presented in detail.

1) Optimizing the beamforming vector: We can update the value of $\mathbf{w}$ at the current $(k+1)$-st iteration, once the values of $\boldsymbol{\theta}_1$ and $\boldsymbol{\phi}_2$ have been found at the previous iteration. To be more specific, given $\boldsymbol{\theta}_1=\boldsymbol{\theta}_1^{[k]}$ and $\boldsymbol{\phi}_2=\boldsymbol{\phi}_2^{[k]}$, we first substitute (16)–(17) into (23) and then rewrite the problem (23) as follows:

$$\max_{\mathbf{w}} \quad \frac{1+P\left|\mathbf{u}_{(\boldsymbol{\theta}_1^{[k]},\boldsymbol{\phi}_2^{[k]})}^{\dagger}\mathbf{w}\right|^2}{1+P\left|\mathbf{v}_{(\boldsymbol{\theta}_1^{[k]},\boldsymbol{\phi}_2^{[k]})}^{\dagger}\mathbf{w}\right|^2} \quad \text{s.t.} \quad \text{tr}(\mathbf{w}\mathbf{w}^{\dagger})=1. \tag{24}$$

Herein, $\mathbf{u}_{(\boldsymbol{\theta}_1^{[k]},\boldsymbol{\phi}_2^{[k]})}$ and $\mathbf{v}_{(\boldsymbol{\theta}_1^{[k]},\boldsymbol{\phi}_2^{[k]})}$ are the realizations of the paramaterized vectors $\mathbf{u}_{(\boldsymbol{\theta}_1,\boldsymbol{\phi}_2)}$ and $\mathbf{v}_{(\boldsymbol{\theta}_1,\boldsymbol{\phi}_2)}$ at the k-th iteration. It has been widely exploited that using the Rayleigh-Ritz theorem [22], the closed-form optimal solution to (24) can be expressed as

$$\mathbf{w}^{[k+1]}=\text{eigv}_{\max}\left\{\left(\mathbf{V}^{[k]}+\frac{1}{P}\mathbf{I}\right)^{-1}\left(\mathbf{U}^{[k]}+\frac{1}{P}\mathbf{I}\right)\right\}, \tag{25}$$

where $\text{eigv}_{\max}(\mathbf{Z})$ denotes the eigenvector corresponding to the *largest* eigenvalue of a certain matrix $\mathbf{Z}$. Note that $\mathbf{U}^{[k]}$ and $\mathbf{V}^{[k]}$ are defined as

$$\mathbf{U}^{[k]}=\mathbf{u}_{(\boldsymbol{\theta}_1^{[k]},\boldsymbol{\phi}_2^{[k]})}\mathbf{u}_{(\boldsymbol{\theta}_1^{[k]},\boldsymbol{\phi}_2^{[k]})}^{\dagger}$$

and

$$\mathbf{V}^{[k]}=\mathbf{v}_{(\boldsymbol{\theta}_1^{[k]},\boldsymbol{\phi}_2^{[k]})}\mathbf{v}_{(\boldsymbol{\theta}_1^{[k]},\boldsymbol{\phi}_2^{[k]})}^{\dagger}.$$

Once the AO algorithm is terminated after K_{iters}, we update the final beamforming solution as $\mathbf{w}_{opt}^{[K_{\text{iters}}]}\leftarrow\mathbf{w}^{[K_{\text{iters}}]}$.

2) Optimizing the first RIS: We first rewrite snr_B in (14) and snr_E in (15) as follows:

$$\text{snr}_B=P\left|\boldsymbol{\eta}_B\boldsymbol{\theta}_1+\widetilde{\eta}_B\right|^2=\alpha_B(\boldsymbol{\theta}_1), \tag{26}$$

$$\text{snr}_E=P\left|\boldsymbol{\eta}_E\boldsymbol{\theta}_1+\widetilde{\eta}_E\right|^2=\alpha_E(\boldsymbol{\theta}_1), \tag{27}$$

where

$$\begin{aligned}
\boldsymbol{\eta}_B&=\left(\xi_1(\boldsymbol{\phi}_2^{[k]})^{\top}\mathbf{B}+\xi_2\mathbf{g}_{BR_1A}\right)\in\mathbb{C}^{1\times N},\\
\widetilde{\eta}_B&=\left(\xi_3(\boldsymbol{\phi}_2^{[k]})^{\top}\mathbf{g}_{BR_2A}+\xi_4\mathbf{h}_{BA}\mathbf{w}^{[k+1]}\right)\in\mathbb{C}^{1\times 1},\\
\boldsymbol{\eta}_E&=\left(\chi_1(\boldsymbol{\phi}_2^{[k]})^{\top}\mathbf{E}+\chi_2\mathbf{g}_{ER_1A}\right)\in\mathbb{C}^{1\times N},\\
\widetilde{\eta}_E&=\left(\chi_3(\boldsymbol{\phi}_2^{[k]})^{\top}\mathbf{g}_{ER_2A}+\chi_4\mathbf{h}_{EA}\mathbf{w}^{[k+1]}\right)\in\mathbb{C}^{1\times 1}.
\end{aligned}$$

Substituting (26) and (27) into (23), we rewrite (23) as

$$\max_{\boldsymbol{\theta}_1} \quad \frac{1+\alpha_B(\boldsymbol{\theta}_1)}{1+\alpha_E(\boldsymbol{\theta}_1)} \quad \text{s.t.} \quad \text{(22b)}. \tag{28}$$

This problem belongs to the family of fractional programming (FP) problems, which can be addressed by using Dinkelbach's method [40], [41]. Hence, we employ Dinkelbach's method for solving (28) in an iterative manner. This means that during the $(k+1)$-st iteration of our AO algorithm, there are multiple *inner*-iterations produced by Dinkelbach's method.[5] Since the AO algorithm has K_{iters} iterations, (28) will be evaluated K_{iters} times by Dinkelbach's method. Let Q be the maximum number of inner-iterations required by Dinkelbach's method. Then, at the $(q+1)$-st inner-iteration of the $(k+1)$-st outer-iteration, we will solve the following inner-problem:

$$\max_{\boldsymbol{\theta}_1} \quad [1+\alpha_B(\boldsymbol{\theta}_1)]-t_1^{[q]}\left[1+\alpha_E(\boldsymbol{\theta}_1)\right] \quad \text{s.t.} \quad \text{(22b)}. \tag{29}$$

Herein, $t_1^{[q]}$ is defined as

$$t_1^{[q]}=\frac{1+\alpha_B(\boldsymbol{\theta}_1^{[k+1,q]})}{1+\alpha_E(\boldsymbol{\theta}_1^{[k+1,q]})} \tag{30}$$

and $\boldsymbol{\theta}_1^{[k+1,q]}$ is the solution at the q-th inner-iteration of the $(k+1)$-st outer-iteration. Note that the initial value of $t_1^{[q]}$ is $t_1^{[0]}=\frac{1+\alpha_B(\boldsymbol{\theta}_1^{[k,Q]})}{1+\alpha_E(\boldsymbol{\theta}_1^{[k,Q]})}$, where $\boldsymbol{\theta}_1^{[k,Q]}$ is the solution found at the *last* inner-iteration of the previous k-th outer-iteration. According to Dinkelbach's method, solving (29) at the $(k+1)$-st outer-iteration will yield the solution $\boldsymbol{\theta}_1^{[k+1,q+1]}$, which is better than the previous solution $\boldsymbol{\theta}_1^{[k+1,q]}$ because $t_1^{[q+1]}>t_1^{[q]}$. The convergence of Dinkelbach's method is characterised in Appendix C.

The problem (29) is the same as the following one:

$$\max_{\boldsymbol{\theta}_1} \quad f_1(\boldsymbol{\theta}_1|t_1^{[q]}) \quad \text{s.t.} \quad \text{(22b)}. \tag{31}$$

Herein, $f_1(\boldsymbol{\theta}_1|t_1^{[q]})$ is defined as

$$\begin{aligned}
f_1(\boldsymbol{\theta}_1|t_1^{[q]})&=\frac{1}{P}\left(\alpha_B(\boldsymbol{\theta}_1)-t_1^{[q]}\alpha_E(\boldsymbol{\theta}_1)\right)\\
&=\left|\boldsymbol{\eta}_B\boldsymbol{\theta}_1+\widetilde{\eta}_B\right|^2-t_1^{[q]}\left|\boldsymbol{\eta}_E\boldsymbol{\theta}_1+\widetilde{\eta}_E\right|^2\\
&=\boldsymbol{\theta}_1^{\dagger}\left(\boldsymbol{\eta}_B^{\dagger}\boldsymbol{\eta}_B-t_1^{[q]}\boldsymbol{\eta}_E^{\dagger}\boldsymbol{\eta}_E\right)\boldsymbol{\theta}_1\\
&\quad+2\,\Re\left\{\left(\widetilde{\eta}_B^{*}\boldsymbol{\eta}_B-t_1^{[q]}\widetilde{\eta}_E^{*}\boldsymbol{\eta}_E\right)\boldsymbol{\theta}_1\right\}\\
&\quad+|\widetilde{\eta}_B|^2-t_1^{[q]}|\widetilde{\eta}_E|^2.
\end{aligned} \tag{32}$$

Proposition 3. *Given $\mathbf{A}\in\mathbb{C}^{M\times N}$, $\mathbf{b}\in\mathbb{C}^{M\times 1}$ and $\mathbf{z}_0\in\mathbb{C}^{M\times 1}$, the following inequality always holds true*

$$\begin{aligned}
\|\mathbf{A}\mathbf{z}+\mathbf{b}\|^2\geq\ &2\,\Re\left\{\left(\mathbf{z}_0^{\dagger}\mathbf{A}^{\dagger}+\mathbf{b}^{\dagger}\right)\mathbf{A}\mathbf{z}\right\}\\
&+\|\mathbf{b}\|^2-\|\mathbf{A}\mathbf{z}_0\|^2,
\end{aligned} \tag{33}$$

where $\mathbf{z}\in\mathbb{C}^{N\times 1}$ is an arbitrary vector. The equality "=" occurs at $\mathbf{z}=\mathbf{z}_0$.

Proof. See Appendix A. □

Let $\lambda_1^{[q]}$ be the maximum eigenvalue of the rank-two Hermitian symmetric matrix $\boldsymbol{\eta}_B^{\dagger}\boldsymbol{\eta}_B-t_1^{[q]}\boldsymbol{\eta}_E^{\dagger}\boldsymbol{\eta}_E$. Then, we have

$$\boldsymbol{\theta}_1^{\dagger}\left(\boldsymbol{\eta}_B^{\dagger}\boldsymbol{\eta}_B-t_1^{[q]}\boldsymbol{\eta}_E^{\dagger}\boldsymbol{\eta}_E\right)\boldsymbol{\theta}_1$$

[5]For readability, we discuss the convergence in Appendix C.

$$
\begin{aligned}
&= \boldsymbol{\theta}_1^\dagger \left(\boldsymbol{\eta}_B^\dagger \boldsymbol{\eta}_B - t_1^{[q]} \boldsymbol{\eta}_E^\dagger \boldsymbol{\eta}_E + |\lambda_1^{[q]}| \mathbf{I}_N \right) \boldsymbol{\theta}_1 - |\lambda_1^{[q]}| \boldsymbol{\theta}_1^\dagger \mathbf{I}_N \boldsymbol{\theta}_1 \\
&\geq 2\,\Re\left\{ (\boldsymbol{\theta}_1^{[k+1,q]})^\dagger \left(\boldsymbol{\eta}_B^\dagger \boldsymbol{\eta}_B - t_1^{[q]} \boldsymbol{\eta}_E^\dagger \boldsymbol{\eta}_E + |\lambda_1^{[q]}| \mathbf{I}_N \right) \boldsymbol{\theta}_1 \right\} \\
&- (\boldsymbol{\theta}_1^{[k+1,q]})^\dagger \left(\boldsymbol{\eta}_B^\dagger \boldsymbol{\eta}_B - t_1^{[q]} \boldsymbol{\eta}_E^\dagger \boldsymbol{\eta}_E \right) \boldsymbol{\theta}_1^{[k+1,q]} - 2|\lambda_1^{[q]}| N,
\end{aligned} \tag{34}
$$

where the inequality is obtained by using Proposition (33) and the constraint (22b).

Based on (32) and (34), we arrive at:

$$
f_1(\boldsymbol{\theta}_1 | t_1^{[q]}) \geq f_1^{[q]}(\boldsymbol{\theta}_1) = 2\,\Re\left\{ \boldsymbol{b}_1^{[q]} \boldsymbol{\theta}_1 \right\} + c_1^{[q]}, \tag{35}
$$

where

$$
\begin{aligned}
\boldsymbol{b}_1^{[q]} &= \widetilde{\eta}_B^* \boldsymbol{\eta}_B - t_1^{[q]} \widetilde{\eta}_E^* \boldsymbol{\eta}_E \\
&+ (\boldsymbol{\theta}_1^{[k+1,q]})^\dagger \left(\boldsymbol{\eta}_B^\dagger \boldsymbol{\eta}_B - t_1^{[q]} \boldsymbol{\eta}_E^\dagger \boldsymbol{\eta}_E + |\lambda_1^{[q]}| \mathbf{I}_N \right),
\end{aligned} \tag{36}
$$

$$
\begin{aligned}
c_1^{[q]} &= |\widetilde{\eta}_B|^2 - t_1^{[q]} |\widetilde{\eta}_E|^2 - 2|\lambda_1^{[q]}| N \\
&- (\boldsymbol{\theta}_1^{[k+1,q]})^\dagger \left(\boldsymbol{\eta}_B^\dagger \boldsymbol{\eta}_B - t_1^{[q]} \boldsymbol{\eta}_E^\dagger \boldsymbol{\eta}_E \right) \boldsymbol{\theta}_1^{[k+1,q]}.
\end{aligned} \tag{37}
$$

Thus, to update $\boldsymbol{\theta}_1^{[k+1,q+1]}$, we solve the minorant maximization problem of (31) as follows:

$$
\max_{\boldsymbol{\theta}_1} \quad f_1^{[q]}(\boldsymbol{\theta}_1) \quad \text{s.t.} \quad \text{(22b)}. \tag{38}
$$

The above problem is maximized when $\Re\left\{ \boldsymbol{b}_1^{[q]} \boldsymbol{\theta}_1 \right\} = |\boldsymbol{b}_1^{[q]} \boldsymbol{\theta}_1|$, which leads to the closed-form solution:

$$
\boldsymbol{\theta}_1^{[k+1,q+1]}(n) = e^{-j \angle \boldsymbol{b}_1^{[q]}}, \; n \in \{1, \ldots, N\}. \tag{39}
$$

After Q inner-iterations, we will update $\boldsymbol{\theta}_{1,opt}^{[k+1]} \leftarrow \boldsymbol{\theta}_1^{[k+1,Q]}$ as the solution of (28). After the entire AO algorithm is terminated, the final solution of the original problem (23) will be $\boldsymbol{\theta}_{1,opt}^{[K_{\text{iters}}]} \leftarrow \boldsymbol{\theta}_1^{[K_{\text{iters}},Q]}$ (not including $\mathbf{w}$ and $\boldsymbol{\phi}_2$).

3) Optimizing the second RIS: Once $\mathbf{w}$ and $\boldsymbol{\theta}_1$ have been found, we can update the value of $\boldsymbol{\phi}_2$. In doing so, we first rewrite snr_B in (14) and snr_E in (15) as

$$
\text{snr}_B = P \left| \boldsymbol{\omega}_B^\top \boldsymbol{\phi}_2 + \widetilde{\omega}_B \right|^2 = \beta_B(\boldsymbol{\phi}_2), \tag{40}
$$

$$
\text{snr}_E = P \left| \boldsymbol{\omega}_E^\top \boldsymbol{\phi}_2 + \widetilde{\omega}_E \right|^2 = \beta_E(\boldsymbol{\phi}_2), \tag{41}
$$

where we have

$$
\begin{aligned}
\boldsymbol{\omega}_B &= (\xi_1 \mathbf{B} \boldsymbol{\theta}_1^{[k+1]} + \xi_3 \mathbf{g}_{BR_2A}) \in \mathbb{C}^{N \times 1}, \\
\widetilde{\omega}_B &= (\xi_2 \mathbf{g}_{BR_1A} \boldsymbol{\theta}_1^{[k+1]} + \xi_4 \mathbf{h}_{BA} \mathbf{w}^{[k+1]}) \in \mathbb{C}^{1 \times 1}, \\
\boldsymbol{\omega}_E &= (\chi_1 \mathbf{E} \boldsymbol{\theta}_1^{[k+1]} + \chi_3 \mathbf{g}_{ER_2A}) \in \mathbb{C}^{N \times 1}, \\
\widetilde{\omega}_E &= (\chi_2 \mathbf{g}_{ER_1A} \boldsymbol{\theta}_1^{[k+1]} + \chi_4 \mathbf{h}_{EA} \mathbf{w}^{[k+1]}) \in \mathbb{C}^{1 \times 1}.
\end{aligned}
$$

Substituting (40) and (41) into (23), we rewrite (23) as

$$
\max_{\boldsymbol{\phi}_2} \quad \frac{1 + \beta_B(\boldsymbol{\phi}_2)}{1 + \beta_E(\boldsymbol{\phi}_2)} \quad \text{s.t.} \quad \text{(22c)}. \tag{42}
$$

Using Dinkelbach's method, we can solve (42) in an iterative manner. Recall that Dinkelbach's method aims for solving a sequence of multiple inner problems. Let Q be the number of inner-iterations required by Dinkelbach's method. At the $(q+1)$-st inner-iteration of the $(k+1)$-st outer-iteration, we will solve the following inner-problem:

$$
\max_{\boldsymbol{\phi}_2} \quad [1 + \beta_B(\boldsymbol{\phi}_2)] - t_2^{[q]} [1 + \beta_E(\boldsymbol{\phi}_2)] \quad \text{s.t.} \quad \text{(22c)}, \tag{43}
$$

where $t_2^{[q]}$ is defined as

$$
t_2^{[q]} = \frac{1 + \beta_B(\boldsymbol{\phi}_2^{[k+1,q]})}{1 + \beta_E(\boldsymbol{\phi}_2^{[k+1,q]})} \tag{44}
$$

and $\boldsymbol{\phi}_2^{[k+1,q]}$ is the solution at the q-th inner-iteration of the same $(k+1)$-th outer-iteration. Let us denote the solution of (43) by $\boldsymbol{\phi}_2^{[k+1,q+1]}$. According to the principle of Dinkelbach's method, $\boldsymbol{\phi}_2^{[k+1,q+1]}$ is a better point than $\boldsymbol{\phi}_2^{[k+1,q]}$ because $t_2^{[q+1]} > t_2^{[q]}$. For further details, please refer to Appendix C.

The problem (43) is the same as the following one:

$$
\max_{\boldsymbol{\phi}_2} \quad f_2(\boldsymbol{\phi}_2 | t_2^{[q]}) \quad \text{s.t.} \quad \text{(22c)}, \tag{45}
$$

where

$$
\begin{aligned}
f_2(\boldsymbol{\phi}_2 | t_2^{[q]}) &= \frac{1}{P} \left(\beta_B(\boldsymbol{\phi}_2) - t_2^{[q]} \beta_E(\boldsymbol{\phi}_2) \right) \\
&= \left| \boldsymbol{\omega}_B^\top \boldsymbol{\phi}_2 + \widetilde{\omega}_B \right|^2 - t_2^{[q]} \left| \boldsymbol{\omega}_E^\top \boldsymbol{\phi}_2 + \widetilde{\omega}_E \right|^2 \\
&= \boldsymbol{\phi}_2^\dagger \left(\boldsymbol{\omega}_B^* \boldsymbol{\omega}_B^\top - t_2^{[q]} \boldsymbol{\omega}_E^* \boldsymbol{\omega}_E^\top \right) \boldsymbol{\phi}_2 \\
&+ 2\,\Re\left\{ \left(\widetilde{\omega}_B^* \boldsymbol{\omega}_B^\top - t_2^{[q]} \widetilde{\omega}_E^* \boldsymbol{\omega}_E^\top \right) \boldsymbol{\phi}_2 \right\} \\
&+ |\widetilde{\omega}_B|^2 - t_2^{[q]} |\widetilde{\omega}_E|^2.
\end{aligned} \tag{46}
$$

Let $\lambda_2^{[q]}$ be the maximum eigenvalue of the rank-two Hermitian symmetric matrix $\boldsymbol{\omega}_B^* \boldsymbol{\omega}_B^\top - t_2^{[q]} \boldsymbol{\omega}_E^* \boldsymbol{\omega}_E^\top$. Then, we have

$$
\begin{aligned}
&\boldsymbol{\phi}_2^\dagger \left(\boldsymbol{\omega}_B^* \boldsymbol{\omega}_B^\top - t_2^{[q]} \boldsymbol{\omega}_E^* \boldsymbol{\omega}_E^\top \right) \boldsymbol{\phi}_2 \\
&= \boldsymbol{\phi}_2^\dagger \left(\boldsymbol{\omega}_B^* \boldsymbol{\omega}_B^\top - t_2^{[q]} \boldsymbol{\omega}_E^* \boldsymbol{\omega}_E^\top + |\lambda_2^{[q]}| \mathbf{I}_N \right) \boldsymbol{\phi}_2 - |\lambda_2^{[q]}| \boldsymbol{\phi}_2^\dagger \mathbf{I}_N \boldsymbol{\phi}_2 \\
&\geq 2\,\Re\left\{ (\boldsymbol{\phi}_2^{[k+1,q]})^\dagger \left(\boldsymbol{\omega}_B^* \boldsymbol{\omega}_B^\top - t_2^{[q]} \boldsymbol{\omega}_E^* \boldsymbol{\omega}_E^\top + |\lambda_2^{[q]}| \mathbf{I}_N \right) \boldsymbol{\phi}_2 \right\} \\
&- (\boldsymbol{\phi}_2^{[k+1,q]})^\dagger \left(\boldsymbol{\omega}_B^* \boldsymbol{\omega}_B^\top - t_2^{[q]} \boldsymbol{\omega}_E^* \boldsymbol{\omega}_E^\top \right) \boldsymbol{\phi}_2^{[k+1,q]} - 2|\lambda_2^{[q]}| N,
\end{aligned} \tag{47}
$$

where the inequality is obtained by using Proposition (33) and the constraint (22c).

Based on (46) and (47), we arrive at:

$$
f_2(\boldsymbol{\phi}_2 | t_2^{[q]}) \geq f_2^{[q]}(\boldsymbol{\phi}_2) = 2\,\Re\left\{ \boldsymbol{b}_2^{[q]} \boldsymbol{\phi}_2 \right\} + c_2^{[q]}, \tag{48}
$$

where

$$
\begin{aligned}
\boldsymbol{b}_2^{[q]} &= \widetilde{\omega}_B^* \boldsymbol{\omega}_B^\top - t_2^{[q]} \widetilde{\omega}_E^* \boldsymbol{\omega}_E^\top \\
&+ (\boldsymbol{\phi}_2^{[k+1,q]})^\dagger \left(\boldsymbol{\omega}_B^* \boldsymbol{\omega}_B^\top - t_2^{[q]} \boldsymbol{\omega}_E^* \boldsymbol{\omega}_E^\top + |\lambda_2^{[q]}| \mathbf{I}_N \right),
\end{aligned} \tag{49}
$$

$$
\begin{aligned}
c_2^{[q]} &= |\widetilde{\omega}_B|^2 - t_2^{[q]} |\widetilde{\omega}_E|^2 - 2|\lambda_2^{[q]}| N \\
&- (\boldsymbol{\phi}_2^{[k+1,q]})^\dagger \left(\boldsymbol{\omega}_B^* \boldsymbol{\omega}_B^\top - t_2^{[q]} \boldsymbol{\omega}_E^* \boldsymbol{\omega}_E^\top \right) \boldsymbol{\phi}_2^{[k+1,q]}
\end{aligned} \tag{50}
$$

To update $\boldsymbol{\phi}_2^{[k+1,q+1]}$, we solve the minorant maximization problem of (45) as follows:

$$
\max_{\boldsymbol{\phi}_2} \quad f_2^{[q]}(\boldsymbol{\phi}_2) \quad \text{s.t.} \quad \text{(22c)}, \tag{51}
$$

Algorithm 1 : The double-RIS AO algorithm

Initialization with feasible $\mathbf{w}^{[0]}$, $\boldsymbol{\theta}_1^{[0]}$ and $\boldsymbol{\phi}_2^{[0]}$
for $0 \le k \le K_{\text{iters}} - 1$ **do**
  Calculate the beamforming vector $\mathbf{w}_{opt}^{[k+1]}$ using (25)
  for $0 \le q \le Q - 1$ **do**
    Calculate the RIS vector $\boldsymbol{\theta}_1^{[k+1,q+1]}$ using (39)
  end for
  Update $\boldsymbol{\theta}_{1,opt}^{[k+1]} \leftarrow \boldsymbol{\theta}_1^{[k+1,Q]}$
  for $0 \le q \le Q - 1$ **do**
    Calculate the RIS vector $\boldsymbol{\phi}_2^{[k+1,q+1]}$ using (52)
  end for
  Update $\boldsymbol{\phi}_{2,opt}^{[k+1]} \leftarrow \boldsymbol{\phi}_2^{[k+1,Q]}$
end for
return $\left(\mathbf{w}_{opt}^{[K_{\text{iters}}]}, \boldsymbol{\theta}_{1,opt}^{[K_{\text{iters}}]}, \boldsymbol{\phi}_{2,opt}^{[K_{\text{iters}}]}\right)$ as the trio of solutions

which admits the closed-form solution

$$\boldsymbol{\phi}_2^{[k+1,q+1]}(n) = e^{-j\angle \boldsymbol{b}_2^{[q]}},\ n \in \{1, \ldots, N\}. \tag{52}$$

After Q inner-iterations, we will update $\boldsymbol{\phi}_{2,opt}^{[k+1]} \leftarrow \boldsymbol{\phi}_2^{[k+1,Q]}$ as the solution of (42). Once the entire AO algorithm is terminated, the final solution of the original problem (23) will be $\boldsymbol{\phi}_{2,opt}^{[K_{\text{iters}}]} \leftarrow \boldsymbol{\phi}_2^{[K_{\text{iters}},Q]}$ (not including $\mathbf{w}$ and $\boldsymbol{\theta}_1$).

C. Complexity Analysis

Let us first define $\mathcal{C}_{\mathbf{w}}^{\text{double}}$ as the complexity of evaluating (25), $\mathcal{C}_{\boldsymbol{\theta}_1}^{\text{double}}$ as the complexity of solving the problem (38), and $\mathcal{C}_{\boldsymbol{\phi}_2}^{\text{double}}$ as the complexity of solving the problem (51). Within each AO iteration, the evaluation of (25) is performed only once, while the inner-convex problems (38) and (51) are solved Q times; thus, the complexity of finding $\mathbf{w}$, $\boldsymbol{\theta}_1$ and $\boldsymbol{\phi}_2$ is $\mathcal{O}\left(\mathcal{C}_{\mathbf{w}}^{\text{double}} + Q(\mathcal{C}_{\boldsymbol{\theta}_1}^{\text{double}} + \mathcal{C}_{\boldsymbol{\phi}_2}^{\text{double}})\right)$. Moreover, the employment of the AO algorithm requires K_{iters} iterations, thus the complexity of the double-RIS AO algorithm can be approximated by $\mathcal{O}\left(K_{\text{iters}}\mathcal{C}_{\mathbf{w}}^{\text{double}} + K_{\text{iters}}Q(\mathcal{C}_{\boldsymbol{\theta}_1}^{\text{double}} + \mathcal{C}_{\boldsymbol{\phi}_2}^{\text{double}})\right)$. In **Algorithm** 1, we summarize the proposed double-RIS AO algorithm.

IV. Benchmark scheme: Solely using a single RIS

In this section, we consider a benchmark scheme, where there is only a single RIS (i.e. R_1) at the ground station. An AO algorithm is also proposed for maximizing the secrecy rate subject to the predetermined constraints.

A. Single-RIS Problem Formulation

Since R_2 is not used in the benchmark scheme, we can express the received signal at B as

$$\begin{aligned}\overline{y}_B = &\sqrt{\Lambda_{BR_1}\Omega_{R_1A}/\sigma_0}\ \mathbf{h}_{BR_1}\mathbf{R}_1\mathbf{H}_{R_1A}\mathbf{w}s \\ &+ \sqrt{\Lambda_{BA}/\sigma_0}\ \mathbf{h}_{BA}\mathbf{w}s + n_B.\end{aligned} \tag{53}$$

Note that $\widetilde{y}_B$ in (53) is deduced from the substitution of $\mathbf{R}_2 = \mathbf{0}$ into (1). Also, we can express the signal received by E as

$$\begin{aligned}\overline{y}_E = &\sqrt{\Lambda_{ER_1}\Omega_{R_1A}/\sigma_0}\ \mathbf{h}_{ER_1}\mathbf{R}_1\mathbf{H}_{R_1A}\mathbf{w}s \\ &+ \sqrt{\Lambda_{EA}/\sigma_0}\ \mathbf{h}_{EA}\mathbf{w}s + n_E\end{aligned} \tag{54}$$

by substituting $\mathbf{R}_2 = \mathbf{0}$ into (2).

Then, the SNRs for B and E in the benchmark scheme can be formulated as follows:

$$\overline{\text{snr}_B} = P \times \left|\xi_2\mathbf{g}_{BR_1A}\boldsymbol{\theta}_1 + \xi_4\mathbf{h}_{BA}\mathbf{w}\right|^2 \triangleq \overline{\alpha}_B(\boldsymbol{\theta}_1), \tag{55}$$

$$\overline{\text{snr}_E} = P \times \left|\chi_2\mathbf{g}_{ER_1A}\boldsymbol{\theta}_1 + \chi_4\mathbf{h}_{EA}\mathbf{w}\right|^2 \triangleq \overline{\alpha}_E(\boldsymbol{\theta}_1), \tag{56}$$

where $\mathbf{g}_{BR_1A}$ and $\mathbf{g}_{ER_1A}$ are defined in (3a) and (3c), respectively. Note that ξ_2, ξ_4, χ_2 and χ_4 are defined right after (5) and (6). Finally, we can formulate the following security optimization problem:

$$\max_{\mathbf{w},\boldsymbol{\theta}_1} \quad \frac{1+\overline{\text{snr}_B}}{1+\overline{\text{snr}_E}} \quad \text{s.t.} \quad \text{(22b), (22d).} \tag{57}$$

For comparison, the result obtained through the benchmark problem (57) will be compared to the result obtained through the proposed double-RIS problem (23).

The AO algorithm presented in this section will be termed as *the single-RIS AO algorithm*. The main difference between the two AO algorithms is that the double-RIS AO algorithm deals with three variables $\mathbf{w}$, $\boldsymbol{\theta}_1$ and $\boldsymbol{\phi}_2$, while the single-RIS AO algorithm only deals with $\mathbf{w}$ and $\boldsymbol{\theta}_1$.

B. The single-RIS AO Algorithm

1) Finding $\mathbf{w}$*:* Let us first define

$$\overline{\mathbf{u}}_{(\boldsymbol{\theta}_1)}^{\dagger} = \xi_2\mathbf{h}_{BR_1}\text{diag}\left(\boldsymbol{\theta}_1\right)\mathbf{H}_{R_1A} + \xi_4\mathbf{h}_{BA}, \tag{58}$$

$$\overline{\mathbf{v}}_{(\boldsymbol{\theta}_1)}^{\dagger} = \chi_2\mathbf{h}_{ER_1}\text{diag}\left(\boldsymbol{\theta}_1\right)\mathbf{H}_{R_1A} + \chi_4\mathbf{h}_{EA}. \tag{59}$$

Then, the single-RIS problem (57) can be rewritten as

$$\max_{\mathbf{w}} \quad \frac{1 + P\left|\overline{\mathbf{u}}_{(\boldsymbol{\theta}_1^{[k]})}^{\dagger}\mathbf{w}\right|^2}{1 + P\left|\overline{\mathbf{v}}_{(\boldsymbol{\theta}_1^{[k]})}^{\dagger}\mathbf{w}\right|^2} \quad \text{s.t.} \quad \text{tr}(\mathbf{w}\mathbf{w}^{\dagger}) = 1. \tag{60}$$

To solve (60), we employ the Rayleigh-Ritz theorem that leads to the following optimal solution:

$$\mathbf{w}^{[k+1]} = \text{eigv}_{\max}\left\{\left(\overline{\mathbf{V}}^{[k]} + \frac{1}{P}\mathbf{I}\right)^{-1}\left(\overline{\mathbf{U}}^{[k]} + \frac{1}{P}\mathbf{I}\right)\right\}, \tag{61}$$

where $\overline{\mathbf{U}}^{[k]} = \overline{\mathbf{u}}_{(\boldsymbol{\theta}_1^{[k]})}\overline{\mathbf{u}}_{(\boldsymbol{\theta}_1^{[k]})}^{\dagger}$ and $\overline{\mathbf{V}}^{[k]} = \overline{\mathbf{v}}_{(\boldsymbol{\theta}_1^{[k]})}\overline{\mathbf{v}}_{(\boldsymbol{\theta}_1^{[k]})}^{\dagger}$.

2) Finding $\boldsymbol{\theta}_1$*:* Given $\mathbf{w} = \mathbf{w}^{[k+1]}$, we rewrite (57) as follows:

$$\max_{\boldsymbol{\theta}_1} \quad \frac{1+\overline{\alpha}_B(\boldsymbol{\theta}_1)}{1+\overline{\alpha}_E(\boldsymbol{\theta}_1)} \quad \text{s.t.} \quad \text{(22b).} \tag{62}$$

Following the same method of solving (28) as in Sub-section III-B2, we can solve (62) by using Dinkelbach's method. To be more specific, we will solve the following inner-problem at the $(q+1)$-st inner-iteration of the $(k+1)$-st outer-iteration:

$$\max_{\boldsymbol{\theta}_1} \quad \left[1+\overline{\alpha}_B(\boldsymbol{\theta}_1)\right] - \bar{t}_1^{[q]}\left[1+\overline{\alpha}_E(\boldsymbol{\theta}_1)\right] \quad \text{s.t.} \quad \text{(22b),} \tag{63}$$

where $\bar{t}_1^{[q]}$ is defined as $\bar{t}_1^{[q]} = \frac{1+\overline{\alpha}_B(\boldsymbol{\theta}_1^{[k+1,q]})}{1+\overline{\alpha}_E(\boldsymbol{\theta}_1^{[k+1,q]})}$, and $\boldsymbol{\theta}_1^{[k+1,q]}$ is the solution at the previous inner-iteration of the same outer-iteration. After solving (63) Q times, we will update $\boldsymbol{\theta}_{1,opt}^{[k+1]} \leftarrow \boldsymbol{\theta}_1^{[k+1,Q]}$ as the solution to (62).

C. Complexity Analysis

In our numerical analysis, some eigenvalue decompositions have to be performed, relying for example on the QR, BR and Lanczos algorithms [42]. Thus, the complexity of computing the eigenvector in (61) depends on the choice of the specific built-in Matlab/Python libraries and packages. At a high level, let us define $\mathcal{C}_{\mathbf{w}}^{\text{single}}$ as the complexity of evaluating (61), and $\mathcal{C}_{\boldsymbol{\theta}_1}^{\text{single}}$ as the complexity of solving the problem (63). Since (63) is solved Q times to find the solution of (62), the complexity of finding $\boldsymbol{\theta}_1$ is $\mathcal{O}\left(Q\mathcal{C}_{\boldsymbol{\theta}_1}^{\text{single}}\right)$. Finally, due to the employment of the AO algorithm, finding $\mathbf{w}$ as well as $\boldsymbol{\theta}_1$ is performed K_{iters} times, the complexity of the single-RIS AO algorithm is approximately given by $\mathcal{O}\left(K_{\text{iters}}\mathcal{C}_{\mathbf{w}}^{\text{single}} + K_{\text{iters}}Q\mathcal{C}_{\boldsymbol{\theta}_1}^{\text{single}}\right)$.

V. Numerical Results

In this section, we present numerical results and compare the security performance of the double-RIS scheme to that of the single-RIS scheme. Unless otherwise stated, the system parameters used for all figures include: the carrier frequency of $f_c = 3$ GHz; Rician factor of $K = 50$ (approx. 17 dB); time delay of $\tau = 10^{-3}$ ms; the number of outer-iterations $K_{\text{iters}} = 10$; the number of inner-iterations $Q = 10$; the velocity of each satellite $\vartheta_{AB} = \vartheta_{AE} = 28000$ km/h; the distances $d_{AB} \approx d_{R_2A} \approx d_{R_1B} \approx d_{R_1R_2} \approx 200$ km, $d_{AE} \approx d_{R_1E} \approx 250$ km, $d_{R_1A} \approx d_{R_2B} \approx 0.1$ km, $d_{R_2E} \approx 245$ km; the noise variance $\sigma_0 = \text{BW} \times \varpi_{\text{Boltzmann}} \times \varpi_{\text{temp}} \times \varpi_{\text{fig}}$, where BW (Hz) is the bandwidth, $\varpi_{\text{Boltzmann}} = 1.38 \times 10^{-23}$ (Joule/Kelvin) is the Boltzmann constant, ϖ_{temp} (Kelvin) is the noise temperature, and ϖ_{fig} (dB) is the noise figure. Upon setting BW $= 20$ MHz, $\varpi_{\text{temp}} = 290$ Kelvin and $\varpi_{\text{fig}} = 10$ dB, we have $\sigma_0 \approx 8 \times 10^{-23}$ W. It should be noted that the carrier frequency f_c can be chosen between 2 GHz and 20 GHz (according to [32]), while the Rician factor should be higher than zero because $K = 0$ indicates that the LoS component does not exist, which is not the case for a space-ground network. Indeed, when a satellite passes over, it becomes visible and there exists a strong LoS component. Additionally, the distances and velocities of the satellites comply with the records in [43], [44]. On the other hand, since the most important variables are the transmit power P, as wel as the number of antennas L, and the number of RIS elements N, we will mainly provide numerical results versus these variables.

A. Performance of Using Double RISs

Figure 2 shows the achievable rates C_B and C_E versus the transmit power P. Observe that increasing the number of antennas will expand the gap between C_B and C_E. To be more specific, the blue dotted curve (i.e. C_B at $L = 1$) and the red curve (i.e. C_E at $L = 1$) are quite close to each other. By contrast, at $L = 3$, the gap between C_B (i.e. the blue dashed curve with square markers) and C_E (i.e. the red dashed curve with square markers) is larger. This implies that the secrecy rate, which relies on the gap between C_B and C_E, will be improved by increasing L. Given that L is also the dimension of the beamforming vector $\mathbf{w}$, the result seen in Fig. 2 addresses the importance of $\mathbf{w}$ in expanding the difference between C_B and C_E, regardless whether we use a single RIS or two RISs.

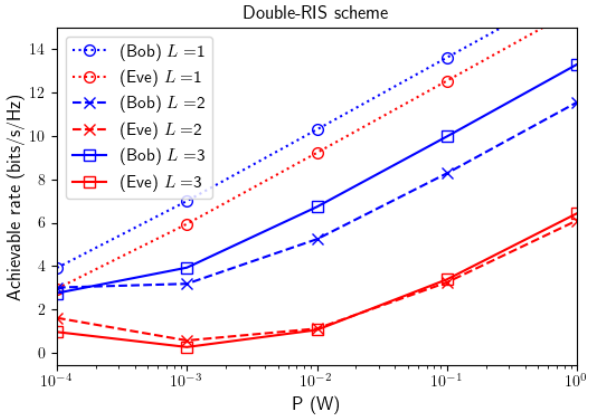

Fig. 2. The achievable rate of legitimate channel, i.e. C_B, and that of eavesdropping channel, i.e. C_E, versus the transmit power P, given that the number of per-RIS elements is $N = 16$.

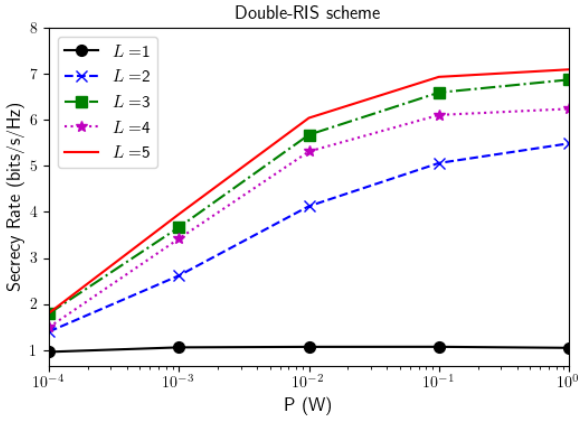

Fig. 3. The secrecy rate C_s versus the transmit power P, given that the number of per-RIS elements is $N = 16$.

Figure 3 shows the secrecy rate C_s versus the transmit power P. Letting the number of antennas L be a parameter that varies, it is plausible that the secrecy rate increases with the transmit power. For $L = 1$, the increase of C_s is insignificant. By contrast, for $L \geq 2$, the increase of C_s becomes more apparent. However, it seems that the rate of the increase of C_s reduces for higher values of L. This might suggest that C_s would reach its upper bound at high L. Additionally, we recall that increasing L will make the AO algorithm more complex, because the search space expands. Hence, it seems unnecessary to use too many antenna elements for security improvement.

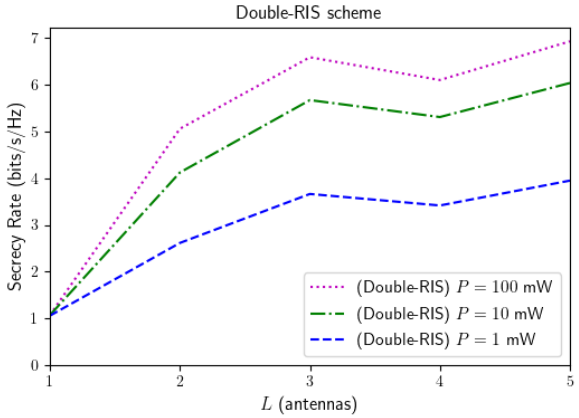

Fig. 4. The secrecy rate C_s versus the transmit power P, given that the number of per-RIS elements is $N = 16$.

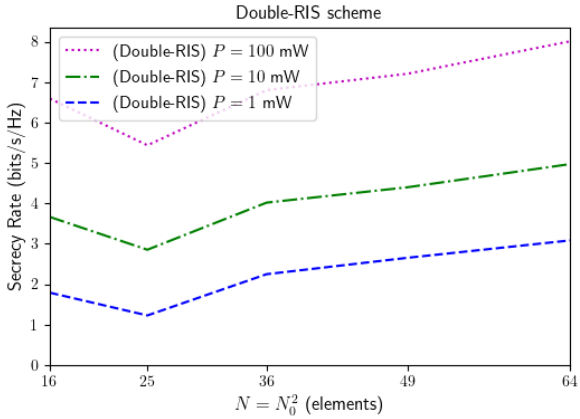

Fig. 5. The secrecy rate C_s versus the number of per-RIS elements N, given that the number of antennas is $L = 3$.

Figure 4 depicts the secrecy rate C_s as a function of the number of antennas L, parameterized by the transmit power P. Observe that the secrecy rate is improved upon increasing the transmit power. Moreover, it is shown that secrecy rate tends to be increased upon increasing the number of antennas, confirming our observation for Figure 2, namely that the secrecy rate is improved by increasing the number of antennas. Note that the solutions found by the AO algorithm may fall within some saddle point. If the saddle point trapping the solutions at $L = 4$ is not significantly better than the one trapping the solution at $L = 3$, it may be expected that the secrecy rate is slightly eroded as shown in Fig. 4. But again, the general trend is still of an increasing nature.

Figure 5 depicts the secrecy rate C_s versus the number of elements N of each RIS. Note that C_s can also be considered as a function of N_0, where N_0 is the number of elements along the horizontal/vertical edge of an RIS grid. Although there is a modest valley at $N = 7^2$, a general upwards trend is observed for a range of N. Although C_s at $N = 6^2$ is higher than C_s at $N = 7^2$, this may be because when N varies from 36 to 49, the search space of the AO algorithm expands and therefore has more saddle points, local maxima and minima. Finally,

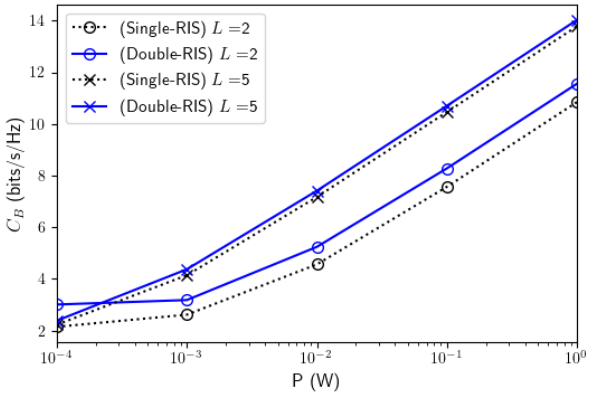

Fig. 6. The achievable rate of legitimate satellite, i.e. C_B, versus the transmit power P in two different schemes, given that the number of per-RIS elements is $N = 16$.

Fig. 5 confirms again that C_s increases with P, regardless of the change of N.

B. Double-RIS versus Single-RIS Scheme

Figures 6–8 show C_B, C_E and C_s versus P, respectively, concerning both the double-RIS scheme and the single-RIS scheme for comparison. It is worth mentioning that the trends of C_B, of C_E and of C_s are *not* strictly monotonic versus P, because all the curves in Fig. 6–8 are drawn based on multiple markers, each corresponding to a value obtained through the AO algorithm's execution. More explicitly, C_B, C_E and C_s are not only dependent of P, but also on the near-optimal solution found by the AO algorithm. C_B, C_E and C_s do not necessarily increase (or decrease) with P all the time. For example, at $P = P_1$, the AO algorithm's execution might yield a near-optimal solution that is worse than the one at $P = P_2$, regardless of $P_1 > P_2$. The details will be presented below.

In Figure 6, the double-RIS scheme is compared to the single-RIS scheme in terms of C_B versus P. To distinguish the two schemes, we denote C_B in the single-RIS case by $C_B^{(1)}$ and C_B in the double-RIS case by $C_B^{(2)}$. In both schemes, we observe that $C_B^{(1)}$ and $C_B^{(2)}$ increase with P and the difference between $C_B^{(1)}$ and $C_B^{(2)}$ increases with L. Indeed, for $L = 2$ antennas, $C_B^{(1)}$ and $C_B^{(2)}$ are almost the same for $P \geq 10^{-2}$ W. However, for $L = 5$ antennas, the gap becomes more distinguishable and it is about 0.35 bits/s/Hz.

In Figure 7, the double-RIS scheme is compared to the single-RIS scheme in terms of C_E versus P. As mentioned earlier, P is not the only factor determining the shape of the C_E curve. Thus, there is a modest valley at $P = 10^{-3}$ W in the both cases. This may be caused by a near-optimal solution, corresponding to $P = 10^{-3}$ W, which is worse than the one corresponding to $P = 10^{-4}$. Moreover, it seems that if P becomes larger (e.g. $P = 10^{-1}$ W or $P = P_{\max} = 1$ W), the influence of P on C_E will become more significant while the influence of the AO algorithm will be slightly reduced. Thus, we can say that in general, C_E increases with P. Additionally, when comparing the double-RIS scheme to the single-RIS

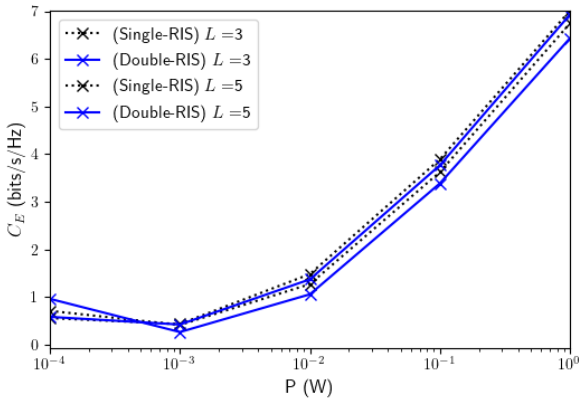

Fig. 7. The achievable rate of undesired satellite, i.e. C_E, versus the transmit power P in two different schemes, given that the number of per-RIS elements is $N = 16$.

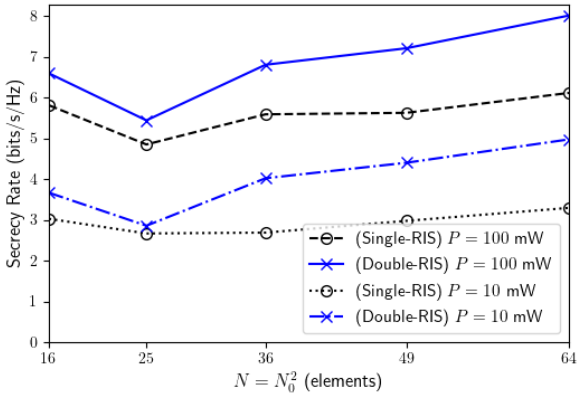

Fig. 9. The secrecy rate C_s versus the number of per-RIS elements N in two different schemes, given that the number of antennas is $L = 3$.

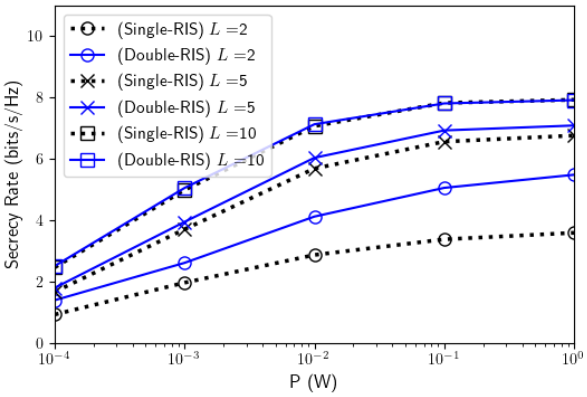

Fig. 8. The secrecy rate C_s versus the transmit power P in two different schemes, given that the number of per-RIS elements is $N = 16$.

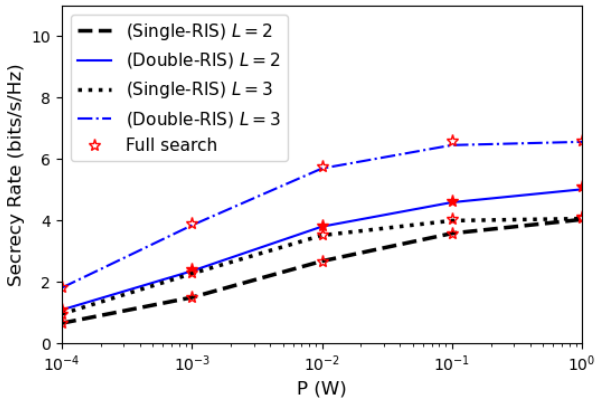

Fig. 10. A comparison between the proposed inner-convex approximation algorithms and the exhaustive search.

scheme, we see that there is no significant difference between $C_E^{(1)}$ and $C_E^{(2)}$, where $C_E^{(1)}$ is C_E in the single-RIS case and $C_E^{(2)}$ is C_E in the double-RIS case.

Figure 8 depicts the secrecy rate C_s versus the transmit power P, parameterized by the number of antennas L. Additionally, the double-RIS scheme is compared to the single-RIS scheme in terms of C_s. Observe that C_s increases both with P and L, regardless whether we employ two RISs or a single one. However, C_s in the double-RIS case (denoted by $C_s^{(2)}$) is higher than C_s in the single-RIS case (denoted by $C_s^{(1)}$). This suggests that the security performance is further improved with the addition of the second RIS. More interestingly, the difference $|C_s^{(2)} - C_s^{(1)}|$ between the two schemes will become more significant, when L increases. For example, for $L = 2$ antennas, $C_s^{(2)}$ is close to $C_s^{(1)}$, but for $L = 10$ antennas, the value of $|C_s^{(2)} - C_s^{(1)}|$ is higher. To elaborate a little further, we recall that the double-RIS AO algorithm considers $\mathbf{w}, \boldsymbol{\theta}_1, \boldsymbol{\phi}_2$, while the single-RIS AO algorithm considers $\mathbf{w}, \boldsymbol{\theta}_1$. Hence, we see that the presence of $\boldsymbol{\phi}_2$ in the double-RIS case improves the performance further. However, the second reflecting vector $\boldsymbol{\phi}_2$ is not the most important factor. Indeed, the beamforming vector $\mathbf{w}$, whose dimension relies on the number of antennas rather than on the RIS size, is a more important factor in determining the security improvement attained.

Figure 9 compares the double-RIS and the single-RIS scheme in terms of C_s versus N. It confirms again the argument that a general upwards trend is observed for a range of N. Moreover, the double-RIS scheme still outperforms its counterpart at any value of N. Indeed, while the single-RIS AO algorithm harnesses only a single reflecting vector $\boldsymbol{\theta}_1$ of size $N \times 1$, the double-RIS AO algorithm harnesses two reflecting vectors $\boldsymbol{\theta}_1$ and $\boldsymbol{\phi}_2$ of $N \times 1$. Thus, the search space in the double-RIS case is larger than in the single-RIS case. Consequently, the rate of change of $C_s^{(2)}$ is higher than that of $C_s^{(1)}$.

Figure 10 compares the exhaustive search to the proposed algorithms in both scenarios (i.e., the single-RIS and double-RIS scenarios). It shows the efficiency of the proposed algorithms in finding near-optimal solutions, which result in a near-optimal security performance. Indeed, the gap between the exhaustive search and both the proposed algorithms becomes insignificant. Moreover, Figure 10 shows that using a pair of Tx & Rx RISs is better than using a single one in terms of

the security attained. Furthermore, increasing the number of transmit antennas improves the security in both cases.

VI. Conclusions

In this paper, we have considered two types of RIS-aided space-ground networks: i) the double-RIS scheme and ii) the single-RIS scheme. In each scheme, an AO algorithm has been proposed for optimizing the beamformer and the RIS reflecting coefficients so that the secrecy rate is maximized. The numerical results have shown that the security level is improved upon increasing the number of antennas L, as well as by increasing the number of per-RIS elements N. The double-RIS scheme outperforms the single-RIS method in terms of security, thus we recommend using two RISs. However, increasing L does not guarantee that the difference between the two schemes will become more significant. This means that the impact of the beamformer at the ground station seems to be higher than that of the RIS reflecting coefficients. On the other hand, the performance difference between the two cases will be augmented upon increasing N. Thus, multiple RISs can be used for improving the security performance when a space-ground network employs a small number of antennas, but the use of multiple RISs may be costly and less effective when the number of antennas is sufficiently large. As an open question, it may be necessary to further explore the theoretical limit of using multiple RISs (i.e., more than two RISs) in future research.

Appendix

A. Proof of Proposition 3

It is obvious that

$$\begin{aligned} 0 &\leq ||(\mathbf{Az}+\mathbf{b})-(\mathbf{Az}_0+\mathbf{b})||^2 \\ &= ||\mathbf{Az}+\mathbf{b}||^2+||(\mathbf{Az}_0+\mathbf{b})||^2||^2 \\ &\quad -2\Re\{(\mathbf{z}_0^\dagger\mathbf{A}^\dagger+\mathbf{b}^\dagger)(\mathbf{Az}+\mathbf{b})\} \\ &= ||\mathbf{Az}+\mathbf{b}||^2-2\Re\{\left(\mathbf{z}_0^\dagger\mathbf{A}^\dagger+\mathbf{b}^\dagger\right)\mathbf{Az}\} \\ &\quad -||\mathbf{b}||^2+||\mathbf{Az}_0||^2, \end{aligned}$$

yielding the inequality (33) and completing the proof.

To illustrate the Proposition 3, please refer to Appendix B for more details.

B. Illustration of Proposition 3

To illustrate Proposition 3, let us commence with a function $f(z) = |z+3|^2$, $-10 \leq z \leq 10$. By Proposition 3, we have $f(z) \geq 2(a+3)z+9-a^2 \triangleq g(z|a)$, where a is a predetermined parameter. The equality occurs at $z=a$, thus the parameter a is also the tangential point. According to the disciplined convex programming (DCP) rules [45], it is impossible to solve the problem $\max_z f(z)$, s.t. $z \in \mathcal{Z} \triangleq \{z \in \mathbb{R}^{1\times 1} | -10 \leq z \leq 10\}$, because the objective function $f(z)$ is a convex function. Instead, we find z that maximizes the lower bound function $g(z|a)$ in an iterative manner. In other words, within a certain iteration, given the parameter a, the inner-approximation problem of $\max_{z\in\mathcal{Z}} g(z|a)$ will be solved. After each iteration, the parameter a will be updated so that the solution is improved. Figure 11 depicts the process

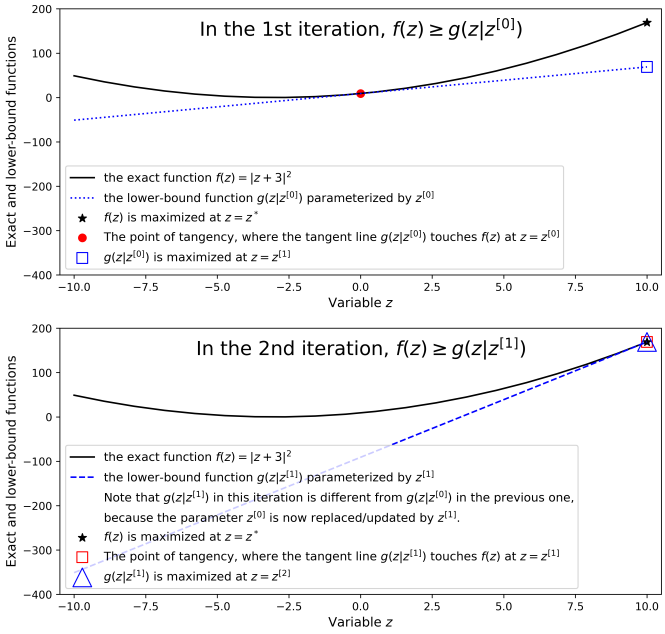

Fig. 11. An illustration of finding near optimal solutions using the first-order Taylor expansion. The tangent line $g(z|a)$ to the curve $f(z)$ is iteratively updated over iterations.

of updating $g(z|a)$ and improving the approximate solution in this example. To be more specific, in the 1-st iteration, starting with $a = z^{[0]}$ (say $z^{[0]} \triangleq 0$), we have $g(z|a=z^{[0]}) = 6z+9$. The solution of the problem $\max_{z\in\mathcal{Z}} g(z|z^{[0]})$ becomes $z = z^{[1]} = 10$, which will be used as the parameter in the next iteration. In the 2-nd iteration, we replace a by $z^{[1]}$ to update the lower bound function of $g(z|a=z^{[1]}) = 26z-91$. Now, the solution becomes $z = z^{[2]} = 10$. Since there is no further improvement, i.e. $|z^{[2]}-z^{[1]}| = 0$, the inner-approximation terminates after as few as two iterations.

Let us consider another example, where the objective function $f(z)$ is the same as in the above example, except that $z \in \mathcal{Z}' \triangleq \{z \in \mathbb{C}^{1\times 1} | -5 \leq \Re\{z\}, \Im\{z\} \leq 10\}$ is now a complex-valued random variable. Figure 12 depicts the process of updating the tangential planes to the curve $f(z)$ and finding near-optimal solutions. Commencing with $a = z^{[0]} = 1-1j$, we have the tangential plane $g(z|z^{[0]}) = 2\Re\{(4+1j)z\}+7$ in the 1-st iteration. The solution $z^{[1]}$ of the problem $\max_{z\in\mathcal{Z}'} g(z|z^{[0]})$ is used as the parameter in the next iteration. After 3 iterations, the near-optimal solution becomes similar to the optimal one.

C. Convergence of Dinkelbach's method

Consider that Dinkelbach's method aims for maximizing a certain concave function $\mathrm{OF}(\mathbf{z}|t) = f(\mathbf{z}) - t^{[q]}g(\mathbf{z})$, where $\mathbf{z}$ is the variable to be optimized and $t^{[q]} = \frac{f(\mathbf{z}^{[q]})}{g(\mathbf{z}^{[q]})}$ is a parameter that relies on the result of the q-th iteration. Herein, $\mathbf{z}^{[q]}$ is the solution obtained at the q-th iteration. Once $\mathrm{OF}(\mathbf{z}|t)$ is maximized at the $(q+1)$-st iteration, we will obtain $\mathbf{z}^{[q+1]}$, which is a better than $\mathbf{z}^{[q]}$ for the following reason:

$$\mathrm{OF}(\mathbf{z}^{[q+1]}|t^{[q]}) \geq \mathrm{OF}(\mathbf{z}^{[q]}|t^{[q]})$$

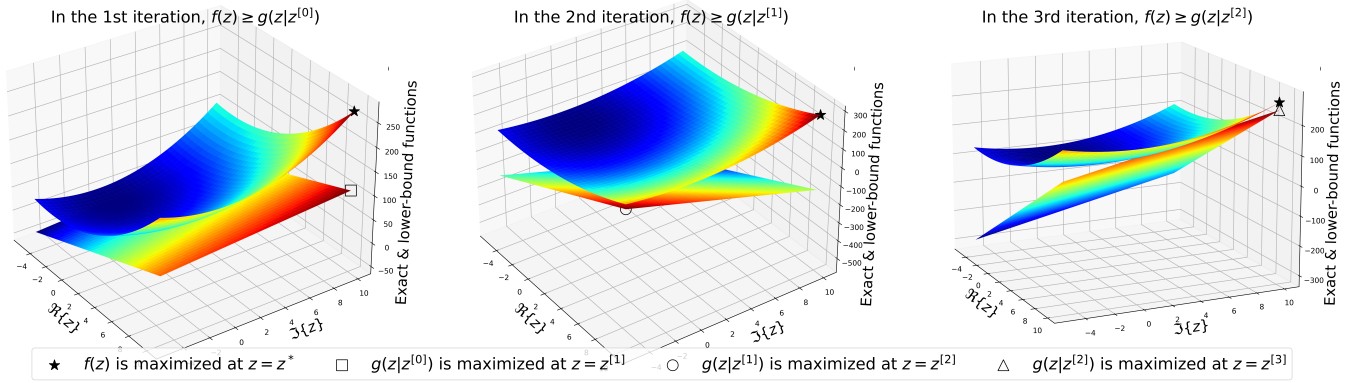

Fig. 12. The tangent plane $g(z|a)$ to the curve $f(z)$ is iteratively updated after each iteration. Herein, we have $a = z^{[0]}$ in the 1-st iteration, $a = z^{[1]}$ in the 2-nd iteration, and $a = z^{[2]}$ in the 3-rd iteration. The near optimal solution $z = z^{[2]}$, which is close to the optimal one z^*, can be found after the 3-rd iteration.

$$\Leftrightarrow f(\mathbf{z}^{[q+1]}) - t^{[q]} g(\mathbf{z}^{[q+1]}) \geq f(\mathbf{z}^{[q]}) - t^{[q]} g(\mathbf{z}^{[q]}). \quad (64)$$

The right-hand side of (64) is equal to 0 due to the definition of $t^{[q]} = \frac{f(\mathbf{z}^{[q]})}{g(\mathbf{z}^{[q]})}$. This implies the following:

$$f(\mathbf{z}^{[q+1]}) - t^{[q]} g(\mathbf{z}^{[q+1]}) \geq 0 \Rightarrow t^{[q]} < \frac{f(\mathbf{z}^{[q+1]})}{g(\mathbf{z}^{[q+1]})}. \quad (65)$$

Once again, substituting $t^{[q]} = \frac{f(\mathbf{z}^{[q]})}{g(\mathbf{z}^{[q]})}$ into (65), we have

$$\frac{f(\mathbf{z}^{[q]})}{g(\mathbf{z}^{[q]})} < \frac{f(\mathbf{z}^{[q+1]})}{g(\mathbf{z}^{[q+1]})}. \quad (66)$$

Since the ratio $\frac{f(\mathbf{z})}{g(\mathbf{z})}$ is what we want to maximize, the inequality (66) implies that the ratio $\frac{f(\mathbf{z})}{g(\mathbf{z})}$ increases after each iteration and thus will converge to the maximal value.

REFERENCES

[1] J. Liu, Y. Shi, Z. M. Fadlullah, and N. Kato, "Space-air-ground integrated network: A survey," *IEEE Communications Surveys Tutorials*, vol. 20, no. 4, pp. 2714–2741, 2018.

[2] M. Srinivasan, S. Gopi, S. Kalyani, X. Huang, and L. Hanzo, "Airplane-aided integrated next-generation networking," *IEEE Transactions on Vehicular Technology*, vol. 70, no. 9, pp. 9345–9354, 2021.

[3] J. Zhang, T. Chen, S. Zhong, J. Wang, W. Zhang, X. Zuo, R. G. Maunder, and L. Hanzo, "Aeronautical *ad hoc* networking for the Internet-above-the-clouds," *Proceedings of the IEEE*, vol. 107, no. 5, pp. 868–911, 2019.

[4] X. Fang, W. Feng, T. Wei, Y. Chen, N. Ge, and C.-X. Wang, "5G embraces satellites for 6G ubiquitous IoT: Basic models for integrated satellite terrestrial networks," *IEEE Internet of Things Journal*, vol. 8, no. 18, pp. 14 399–14 417, 2021.

[5] S. Xu, J. Liu, T. K. Rodrigues, and N. Kato, "Envisioning intelligent reflecting surface empowered space-air-ground integrated network," *IEEE Network*, vol. 35, no. 6, pp. 225–232, 2021.

[6] D. Zhou, M. Sheng, J. Wu, J. Li, and Z. Han, "Gateway placement in integrated satelliteterrestrial networks: Supporting communications and internet of remote things," *IEEE Internet of Things Journal*, vol. 9, no. 6, pp. 4421–4434, 2022.

[7] Y. Zou, J. Zhu, X. Wang, and L. Hanzo, "A survey on wireless security: Technical challenges, recent advances, and future trends," *Proceedings of the IEEE*, vol. 104, no. 9, pp. 1727–1765, 2016.

[8] E. Bjornson and L. Sanguinetti, "Power scaling laws and near-field behaviors of massive MIMO and intelligent reflecting surfaces," *IEEE Open Journal of the Communications Society*, vol. 1, pp. 1306–1324, 2020.

[9] L. You, J. Xiong, D. W. K. Ng, C. Yuen, W. Wang, and X. Gao, "Energy efficiency and spectral efficiency tradeoff in RIS-aided multiuser MIMO uplink transmission," *IEEE Transactions on Signal Processing*, vol. 69, pp. 1407–1421, 2021.

[10] L. Yang, J. Yang, W. Xie, M. O. Hasna, T. Tsiftsis, and M. D. Renzo, "Secrecy performance analysis of RIS-aided wireless communication systems," *IEEE Transactions on Vehicular Technology*, vol. 69, no. 10, pp. 12 296–12 300, 2020.

[11] Z. Tang, T. Hou, Y. Liu, J. Zhang, and C. Zhong, "A novel design of RIS for enhancing the physical layer security for RIS-aided NOMA networks," *IEEE Wireless Communications Letters*, vol. 10, no. 11, pp. 2398–2401, 2021.

[12] Z. Zhang, C. Zhang, C. Jiang, F. Jia, J. Ge, and F. Gong, "Improving physical layer security for reconfigurable intelligent surface aided NOMA 6G networks," *IEEE Transactions on Vehicular Technology*, vol. 70, no. 5, pp. 4451–4463, 2021.

[13] J. Luo, F. Wang, S. Wang, H. Wang, and D. Wang, "Reconfigurable intelligent surface: Reflection design against passive eavesdropping," *IEEE Transactions on Wireless Communications*, vol. 20, no. 5, pp. 3350–3364, 2021.

[14] J. Zhang, H. Du, Q. Sun, B. Ai, and D. W. K. Ng, "Physical layer security enhancement with reconfigurable intelligent surface-aided networks," *IEEE Transactions on Information Forensics and Security*, vol. 16, pp. 3480–3495, 2021.

[15] L. Dong, H.-M. Wang, and J. Bai, "Active reconfigurable intelligent surface aided secure transmission," *IEEE Transactions on Vehicular Technology*, vol. 71, no. 2, pp. 2181–2186, 2022.

[16] S. Hong, C. Pan, H. Ren, K. Wang, and A. Nallanathan, "Artificial-noise-aided secure MIMO wireless communications via intelligent reflecting surface," *IEEE Transactions on Communications*, vol. 68, no. 12, pp. 7851–7866, 2020.

[17] X. Tang, X. Lan, D. Zhai, R. Zhang, and Z. Han, "Securing wireless transmissions with RIS-receiver coordination: Passive beamforming and active jamming," *IEEE Transactions on Vehicular Technology*, vol. 70, no. 6, pp. 6260–6265, 2021.

[18] J. Li, S. Xu, J. Liu, Y. Cao, and W. Gao, "Reconfigurable intelligent surface enhanced secure aerial-ground communication," *IEEE Transactions on Communications*, vol. 69, no. 9, pp. 6185–6197, 2021.

[19] S. Li, B. Duo, M. D. Renzo, M. Tao, and X. Yuan, "Robust secure UAV communications with the aid of reconfigurable intelligent surfaces," *IEEE Transactions on Wireless Communications*, vol. 20, no. 10, pp. 6402–6417, 2021.

[20] F. Shu, Y. Teng, J. Li, M. Huang, W. Shi, J. Li, Y. Wu, and J. Wang, "Enhanced secrecy rate maximization for directional modulation networks via IRS," *IEEE Transactions on Communications*, pp. 1–1, 2021.

[21] W. Shi, X. Zhou, L. Jia, Y. Wu, F. Shu, and J. Wang, "Enhanced secure wireless information and power transfer via intelligent reflecting surface," *IEEE Communications Letters*, vol. 25, no. 4, pp. 1084–1088, 2021.

[22] L. Dong, H.-M. Wang, J. Bai, and H. Xiao, "Double intelligent reflecting surface for secure transmission with inter-surface signal reflection," *IEEE Transactions on Vehicular Technology*, vol. 70, no. 3, pp. 2912–2916, 2021.

[23] Y. Ai, F. A. P. deFigueiredo, L. Kong, M. Cheffena, S. Chatzinotas, and B. Ottersten, "Secure vehicular communications through reconfigurable intelligent surfaces," *IEEE Transactions on Vehicular Technology*, vol. 70, no. 7, pp. 7272–7276, 2021.

[24] H. Niu, Z. Chu, F. Zhou, C. Pan, D. W. K. Ng, and H. X. Nguyen, "Double intelligent reflecting surface-assisted multi-user MIMO mmwave systems with hybrid precoding," *IEEE Transactions on Vehicular Technology*, vol. 71, no. 2, pp. 1575–1587, 2022.

[25] K. Ardah, S. Gherekhloo, A. L. F. de Almeida, and M. Haardt, "Double-RIS versus single-RIS aided systems: Tensor-based MIMO channel estimation and design perspectives," in *IEEE Int. Conf. on Acoustics, Speech and Sig. Proces. (ICASSP)*, 2022, pp. 5183–5187.

[26] S. Xu, J. Liu, and Y. Cao, "Intelligent reflecting surface empowered physical-layer security: Signal cancellation or jamming?" *IEEE Internet of Things Journal*, vol. 9, no. 2, pp. 1265–1275, 2022.

[27] K. Guo and K. An, "On the performance of RIS-assisted integrated satellite-UAV-terrestrial networks with hardware impairments and interference," *IEEE Wireless Communications Letters*, vol. 11, no. 1, pp. 131–135, 2022.

[28] K. Tekbiyik, G. K. Kurt, and H. Yanikomeroglu, "Energy-efficient RIS-assisted satellites for IoT networks," *IEEE Internet of Things Journal*, pp. 1–1, 2021.

[29] H. Niu, Z. Lin, K. An, X. Liang, Y. Hu, D. Li, and G. Zheng, "Active RIS-assisted secure transmission for cognitive satellite terrestrial networks," *IEEE Transactions on Vehicular Technology*, pp. 1–6, 2022.

[30] Z. Lin, H. Niu, K. An, Y. Wang, G. Zheng, S. Chatzinotas, and Y. Hu, "Refracting RIS-aided hybrid satellite-terrestrial relay networks: Joint beamforming design and optimization," *IEEE Transactions on Aerospace and Electronic Systems*, vol. 58, no. 4, pp. 3717–3724, 2022.

[31] S. Xu, J. Liu, T. K. Rodrigues, and N. Kato, "Robust multiuser beamforming for IRS-enhanced near-space downlink communications coexisting with satellite system," *IEEE Internet of Things Journal*, vol. 9, no. 16, pp. 14 900–14 912, 2022.

[32] 3GPP, "Study on new radio (NR) to support non-terrestrial networks," in *Release 15*, 2020.

[33] Y. Chen, M. Wen, L. Wang, W. Liu, and L. Hanzo, "SINR-outage minimization of robust beamforming for the non-orthogonal wireless downlink," *IEEE Transactions on Communications*, vol. 68, no. 11, pp. 7247–7257, 2020.

[34] H. Guo, Z. Yang, Y. Zou, M. Qian, J. Zhu, and L. Hanzo, "Joint optimization of power splitting and beamforming in energy harvesting cooperative networks," *IEEE Transactions on Communications*, vol. 67, no. 12, pp. 8247–8257, 2019.

[35] M. Ding and S. D. Blostein, "MIMO minimum total MSE transceiver design with imperfect CSI at both ends," *IEEE Transactions on Signal Processing*, vol. 57, no. 3, pp. 1141–1150, 2009.

[36] S. Noh, M. D. Zoltowski, Y. Sung, and D. J. Love, "Pilot beam pattern design for channel estimation in massive MIMO systems," *IEEE Journal of Selected Topics in Signal Processing*, vol. 8, no. 5, pp. 787–801, 2014.

[37] D. Dardari and N. Decarli, "Holographic communication using intelligent surfaces," *IEEE Communications Magazine*, vol. 59, no. 6, pp. 35–41, 2021.

[38] A. Pizzo, T. L. Marzetta, and L. Sanguinetti, "Spatially-stationary model for holographic MIMO small-scale fading," *IEEE Journal on Selected Areas in Communications*, vol. 38, no. 9, pp. 1964–1979, 2020.

[39] E. Bjornson and L. Sanguinetti, "Rayleigh fading modeling and channel hardening for reconfigurable intelligent surfaces," *IEEE Wireless Communications Letters*, vol. 10, no. 4, pp. 830–834, 2021.

[40] J.-P. Crouzeix and J. A. Ferland, "Algorithms for generalized fractional programming," *Mathematical Programming*, vol. 52, no. 1, pp. 191–207, 1991.

[41] S. Schaible, "Fractional programming. ii, on dinkelbach's algorithm," *Management Science*, vol. 22, no. 8, pp. 868–873, 1976.

[42] J. Ma, Z. Dong, and P. Zhang, "Comparison of BR and QR eigenvalue algorithms for power system small signal stability analysis," *IEEE Transactions on Power Systems*, vol. 21, no. 4, pp. 1848–1855, 2006.

[43] T. Schonherr, K. Komurasaki, F. Romano, B. Massuti-Ballester, and G. Herdrich, "Analysis of atmosphere-breathing electric propulsion," *IEEE Transactions on Plasma Science*, vol. 43, no. 1, pp. 287–294, 2015.

[44] P. Crandall and R. E. Wirz, "Air-breathing electric propulsion: mission characterization and design analysis," *Journal of Electric Propulsion, Springer*, vol. 1, no. 1, pp. 1–31, 2022.

[45] M. Grant, S. Boyd, and Y. Ye, "CVX: Matlab software for disciplined convex programming," 2008.